International Journal of Mechanical System Dynamics

WILEY

IJMSD International Journal of Mechanical System Dynamics Open Access

RESEARCH ARTICLE OPEN ACCESS

Monitoring of Corrosion Damage by Using iFEM Methodology

Yildirim Dirik | Selda Oterkus | Erkan Oterkus

Department of Naval Architecture, Ocean and Marine Engineering, University of Strathclyde, Glasgow, Scotland

Correspondence: Selda Oterkus (selda.oterkus@strath.ac.uk)

Received: 8 March 2025 | **Revised:** 7 April 2025 | **Accepted:** 9 April 2025

Funding: We would like to thank Babcock International Group for its financial support of the project.

Keywords: corrosion | damage | iFEM | monitoring | sensor

ABSTRACT

Marine environment is a harsh environment that can cause major issues for marine structures while operating in this environment, including fatigue cracking and corrosion damage, which can yield catastrophic consequences, such as human life losses, financial losses, environmental pollution, and so forth. Therefore, it is critical to take necessary actions before undesired situations happen. One potential solution is to install structural health monitoring systems on marine structures. Structural health monitoring is a technology to enhance the safety, stability, and functionality of large engineering structures. The inverse Finite Element Method (iFEM) is a promising technique for this purpose. In this study, the corrosion damage detection capability of iFEM is presented by introducing two new damage parameters for plates under tension and bending loading conditions. The contribution of newly introduced parameters to the accuracy of iFEM on damage detection is demonstrated for multiple corrosion scenarios and sensor configurations.

1 | Introduction

Marine environment is a harsh environment which can cause major issues for marine structures when operating in this environment. One common failure mode seen in marine structures is fatigue damage due to the cyclic loading acting on the structures. Another common failure mode is corrosion damage, which can occur in the form of uniform corrosion and localized corrosion. Uniform corrosion can lead to a reduction in the thickness of the structure for a larger area, whereas localized corrosion causes high stress concentrations, which can act as initiation locations for cracks that can yield catastrophic consequences, such as human life losses, financial losses, environmental pollution, and so forth. Therefore, it is critical to take necessary actions before undesired situations happen. One potential solution is to install structural health monitoring (SHM) systems on marine structures.

There are various SHM tools available for corrosion detection presented in the literature. Katsoudas et al. [1] developed a SHM tool for corrosion-induced thickness loss in marine plates subjected to random loads by using detection theory and Artificial Neural Networks. Tan et al. [2] introduced an early corrosion detection SHM system based on a Fiber Bragg grating-based sensing system. Simmers Jr. et al. [3] proposed an approach to detect corrosion damage using a piezoelectric impedance-based SHM technique. As an alternative approach, inverse Finite Element Method (iFEM) can be considered for corrosion detection. iFEM was introduced by Tessler and Spangler [4] for SHM of aerospace structures. iFEM has various advantages, such as not requiring loading information, which is difficult to measure in operational conditions. Moreover, it can be applied to complex structures, such as marine structures. In addition, it is fast and robust, which makes it applicable for real-time conditions.

https://doi.org/10.1002/msd2.70032

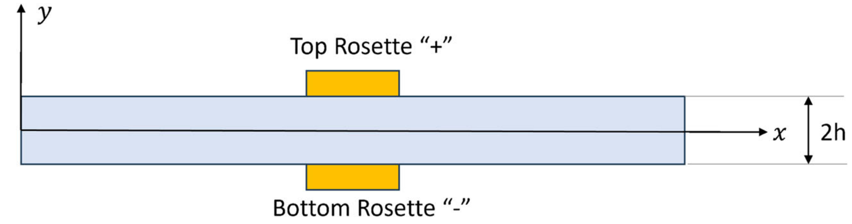

FIGURE 1 | Rosette placement of the shell structure with a thickness of 2 h.

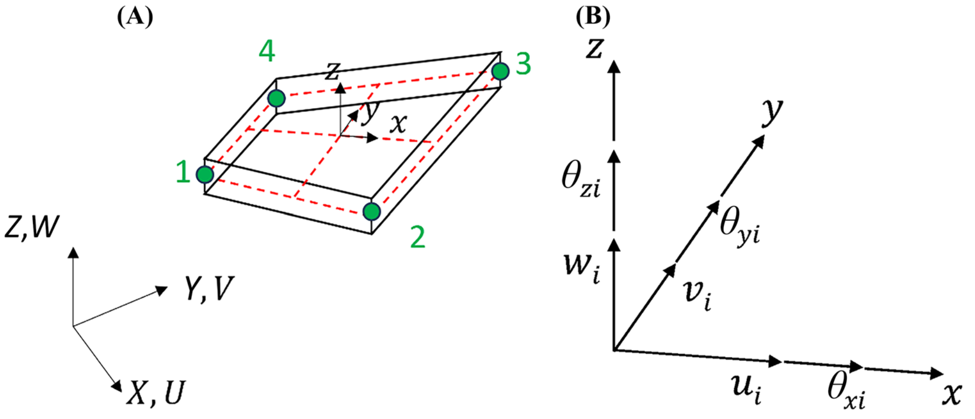

FIGURE 2 | (A) iQS4 element and its local coordinate system defined at the centroid. (B) The defined degrees of freedom at each node in accordance with the local coordinates.

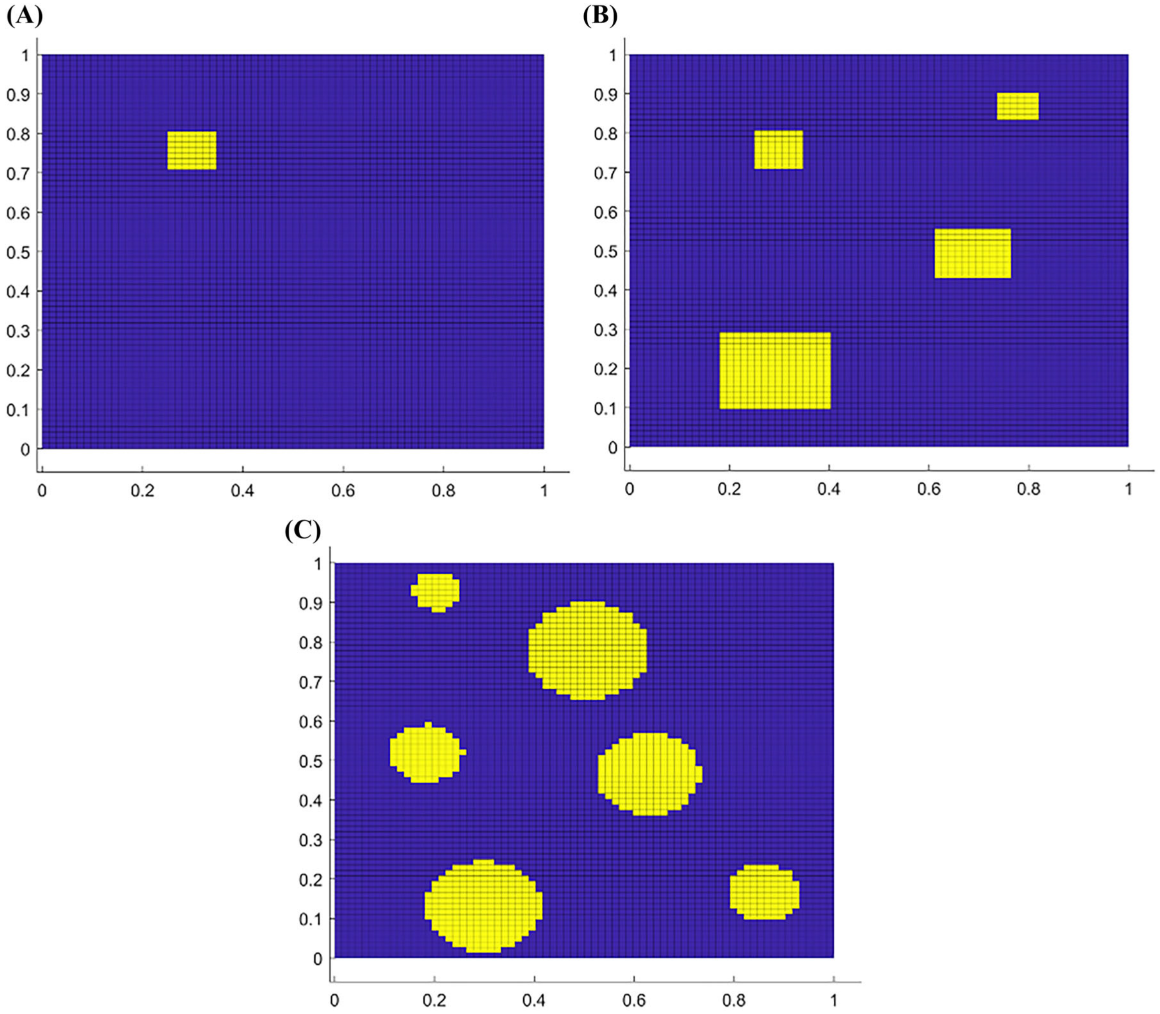

FIGURE 3 | Corrosion scenarios: (A) Case 1, (B) Case 2, and (C) Case 3.

There has been significant progress on iFEM, especially during recent years. Wang et al. [5] monitored the pipeline deformation using iFEM. Tessler et al. [6] used iFEM for shape sensing of plate and shell structures undergoing large displacements. Roy and Gherlone [7] developed a new approach for detecting different types of damage in composite structures based on iFEM. Cerracchio et al. [8] utilized iFEM for real-time monitoring of a composite stiffened panel subjected to mechanical and thermal loads. Kefal et al. [9] presented iFEM for displacement and stress monitoring of composite and sandwich structures. Craiu and Nedelcu [10] combined iFEM and Generalized Beam Theory for accurate shape sensing and damage detection in truncated conical shells. De Mooij et al. [11] developed three-dimensional (3D) iFEM solid elements and considered benchmark cases. Chen et al. [12] reconstructed the multiload strain field of ship stiffened plates based on iFEM. Zhao et al. [13] combined iFEM and third-order shear deformation theory for geometrically nonlinear

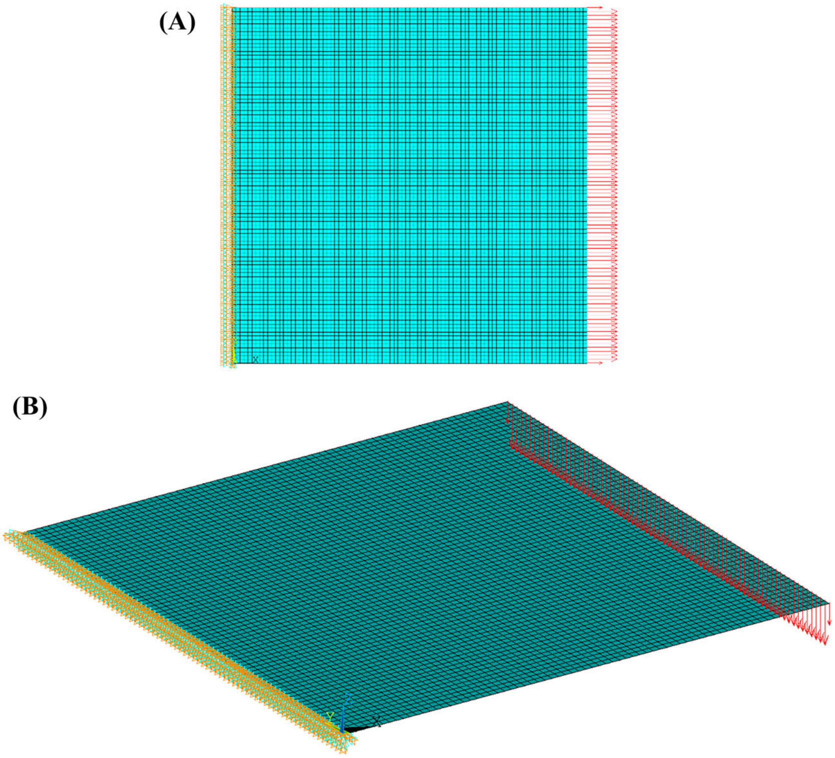

FIGURE 4 | Reference FEM model involving 72 element × 72 element. (A) Tension loading and (B) bending loading. FEM, finite element method.

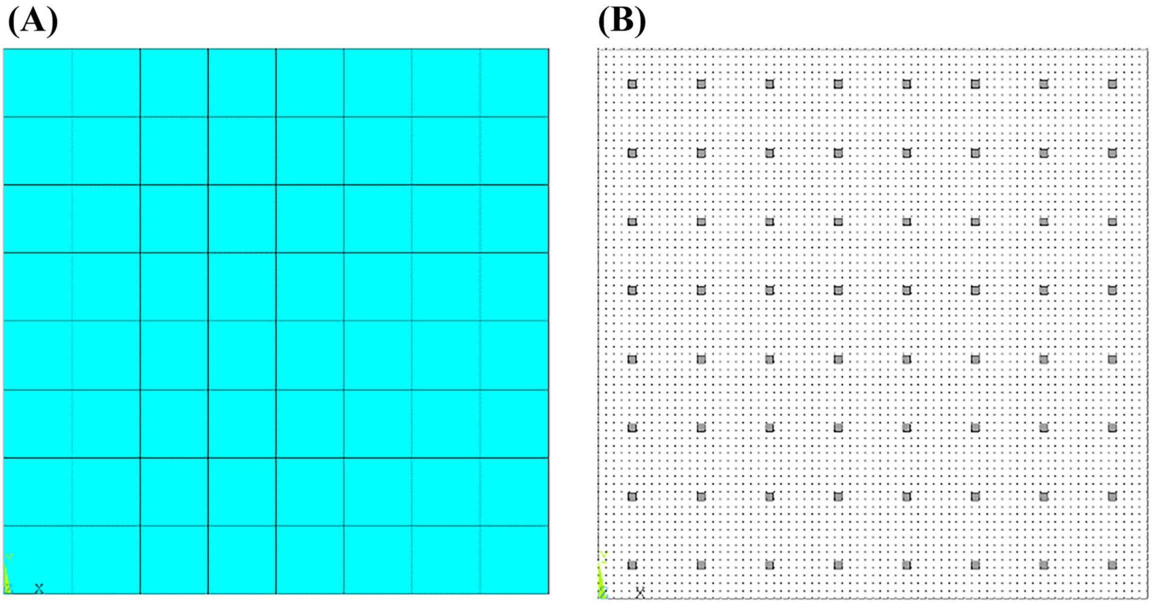

FIGURE 5 | (A) iFEM mesh with 8 × 8 elements and (B) 8 × 8 sensors for the iFEM model. iFEM, inverse finite element method.

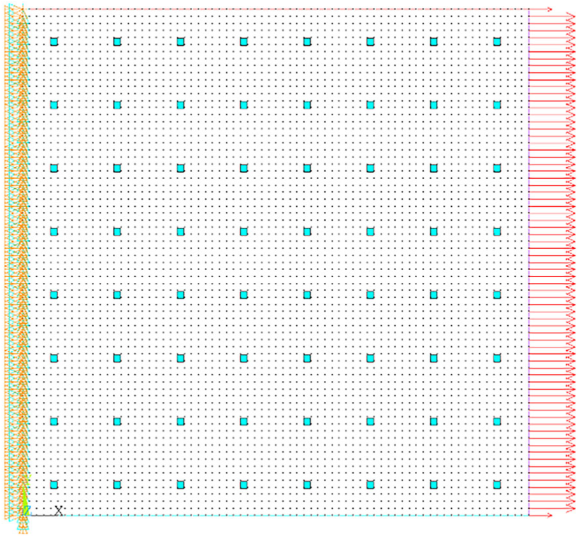

FIGURE 6 | An 8 × 8 sensor configuration and the distributed in-plane loading of 10 kN on the right edge.

shape sensing of anisotropic composite beams. Kefal et al. [14] developed a new quadrilateral inverse-shell element with drilling degrees of freedom (DOF), and this element was used for iFEM analysis of different types of marine structures, including containership [15], chemical tanker [16], bulk carrier [17], and offshore wind turbines [18]. Khalid et al. [19] used the quadrilateral inverse plate element for SHM of thin plate structures. Kefal and Oterkus [20] introduced isogeometric iFEM analysis of thin shell structures, and based on this concept, Dirik et al. [21] developed isogeometric Mindlin–Reissner inverse-shell element formulation for complex stiffened shell structures.

In this study, we present an application of iFEM for the identification of corrosion damage. To achieve this, only strain sensors are utilized, and two new damage parameters are introduced for an accurate identification of the corrosion damage. Various corrosion damage scenarios are considered to validate and demonstrate the capability of the proposed approach.

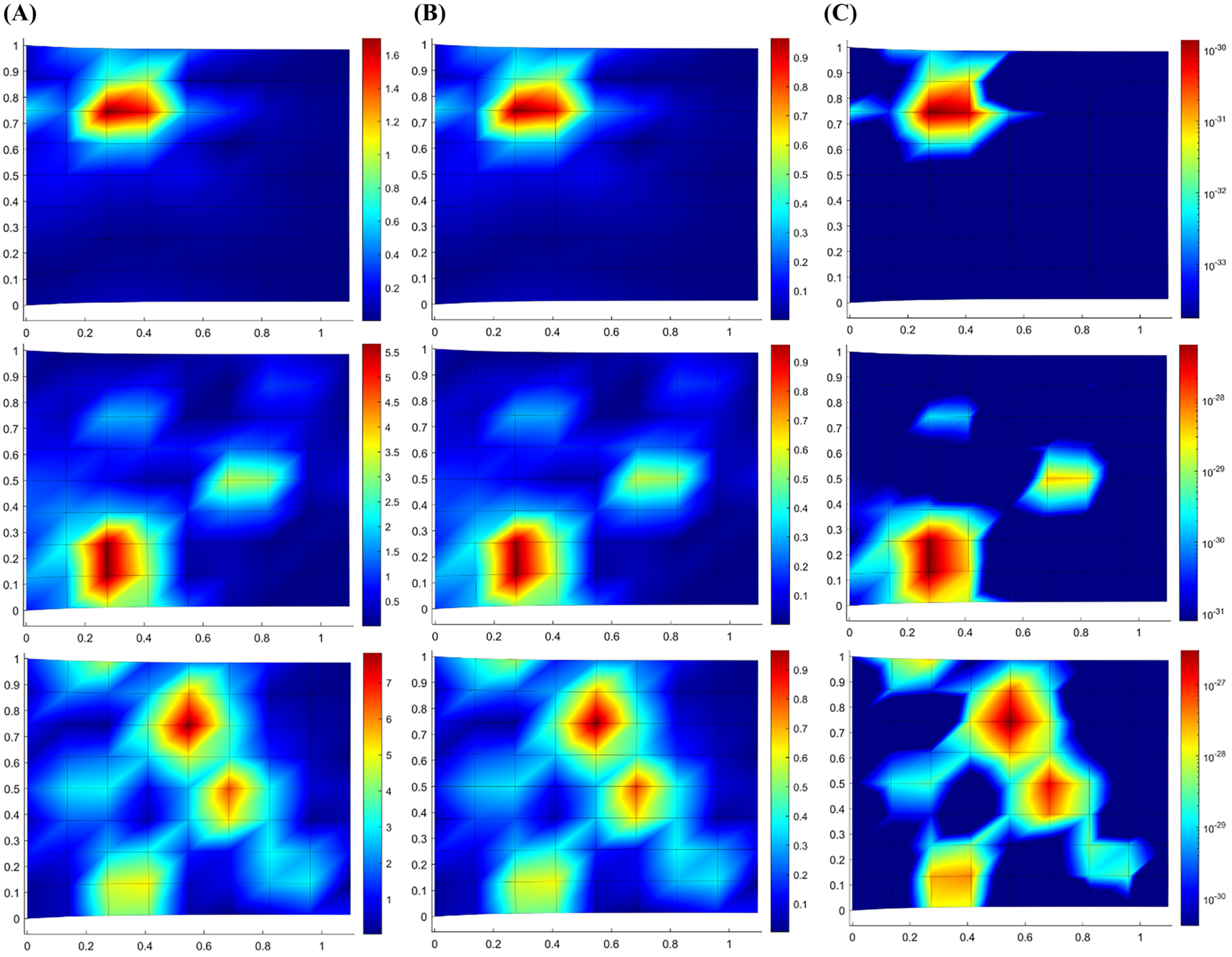

FIGURE 7 | Tension loading case for 8 × 8 sensors and mesh configuration by considering 10% thickness reduction. (A) PDP, (B) RDP, and (C) LDP from top row to bottom row for Case 1, Case 2, and Case 3. LDP, logarithmic damage parameter; PDP, percentage damage parameter; RDP, relative damage parameter.

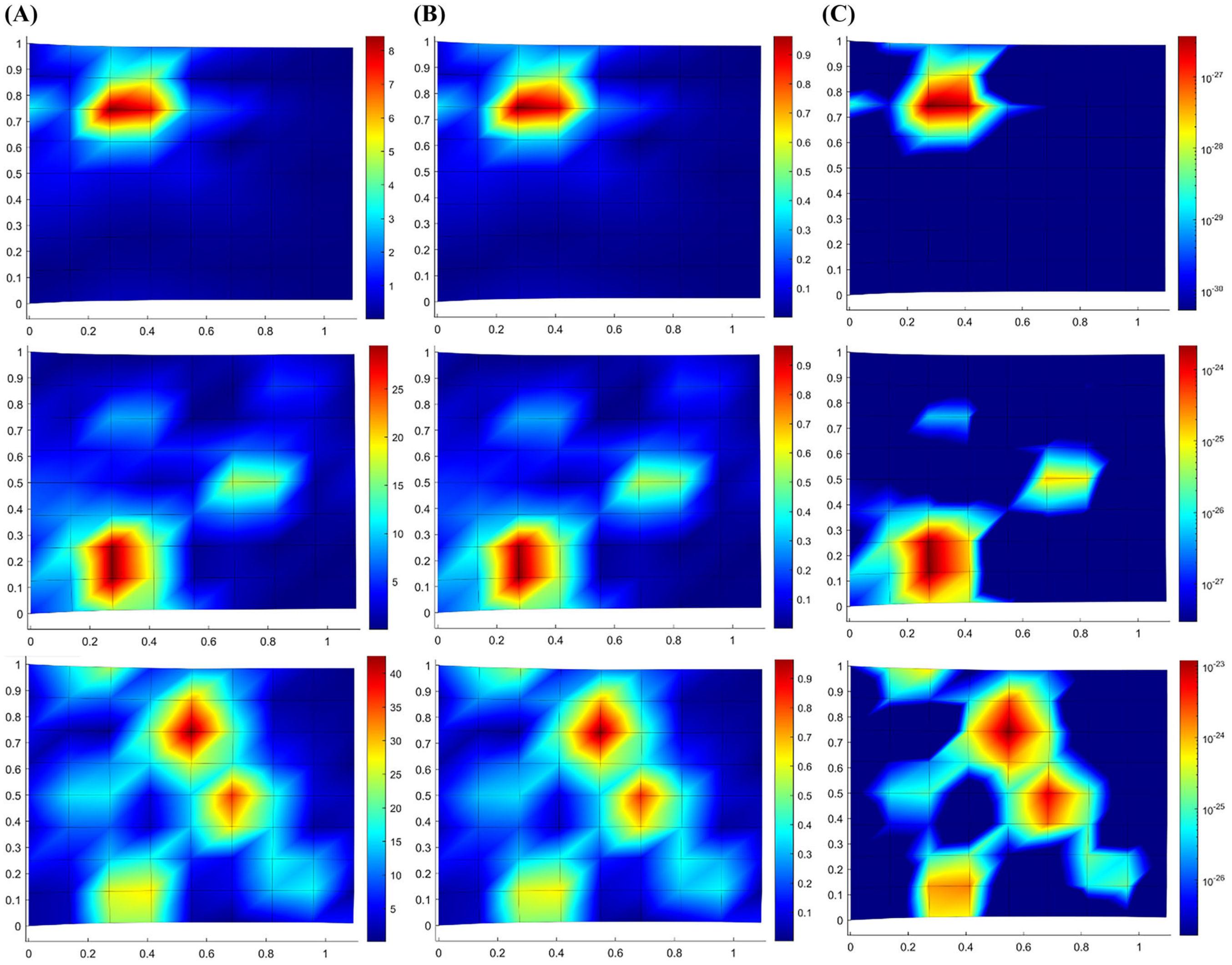

FIGURE 8 | Tension loading case for 8 × 8 sensors and mesh configuration by considering 40% thickness reduction. (A) PDP, (B) RDP, and (C) LDP from top row to bottom row for Case 1, Case 2, and Case 3. LDP, logarithmic damage parameter; PDP, percentage damage parameter; RDP, relative damage parameter.

2 | Methodology: iFEM Formulation

2.1 | iFEM Methodology

The first step of the iFEM analysis is the discretization of the target geometry by using inverse elements. Since iFEM utilizes strain data to calculate the full-field deformation of the geometry, the strain data are collected from the target structure by using in situ strain sensors placed at top and bottom sides of the shell components to feed the inverse elements.

Once the strain data are collected from the selected locations of the target structure, the midplane membrane strains and bending curvatures are calculated by using the measured strain data as

$$\boldsymbol{E}_i \equiv \begin{Bmatrix} E_1 \\ E_2 \\ E_3 \end{Bmatrix}_i = \frac{1}{2}\begin{Bmatrix} \varepsilon_{11}^{+} + \varepsilon_{11}^{-} \\ \varepsilon_{22}^{+} + \varepsilon_{22}^{-} \\ \gamma_{12}^{+} + \gamma_{12}^{-} \end{Bmatrix}_i \quad (i = 1 \cdots n), \tag{1}$$

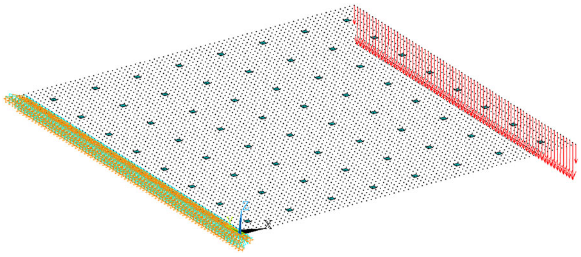

FIGURE 9 | An 8 × 8 sensor configuration and the distributed transverse loading of 1 kN on the right edge.

$$\boldsymbol{K}_i \equiv \begin{Bmatrix} K_4 \\ K_5 \\ K_6 \end{Bmatrix}_i = \frac{1}{2h}\begin{Bmatrix} \varepsilon_{11}^{+} - \varepsilon_{11}^{-} \\ \varepsilon_{22}^{+} - \varepsilon_{22}^{-} \\ \gamma_{12}^{+} - \gamma_{12}^{-} \end{Bmatrix}_i \quad (i = 1 \cdots n), \tag{2}$$

where n stands for the number of sensor sets located at the top and bottom surfaces of the plate, as shown in Figure 1.

Besides membrane strains $\boldsymbol{E}$ and bending curvatures $\boldsymbol{K}$, a straightforward calculation for transverse shear strains $\boldsymbol{G}$ is not possible. Available methods for calculating transverse shear strains by using measured strains are present in the literature, such as Lancaster and Kestutis [22] and Tessler et al. [23, 24]. However, it is possible to assume the plane-stress condition for the target structures, as the majority of marine structures are made of thin shells. Therefore, it is sufficiently safe to ignore the measurement of transverse shear strains for the analysis.

$$\boldsymbol{G}_i \equiv \begin{Bmatrix} G_7 \\ G_8 \end{Bmatrix}_i \quad (i = 1 \cdots n). \tag{3}$$

2.2 | Weighted Least-Squares Functional

A least-squares functional Φ^e for each inverse element is calculated using the measured element strains ε_k^e and analytical section strains ε_k, where k indicates the number of independent strain constituents obtained in accordance with the implemented structural theory for the corresponding inverse element as

$$\Phi^e(\boldsymbol{u}) = \sum_k w_k^e \Phi_k^e, \tag{4}$$

where $\boldsymbol{u}$ is the vector of the element's nodal displacements and Φ_k^e is defined as

$$\Phi_k^e \equiv \frac{1}{n}\sum_{i=1}^{n}\left[\varepsilon_{k(i)}(\boldsymbol{u}^e) - \varepsilon_{k(i)}^e\right]^2. \tag{5}$$

For each inverse element, n number of measured strain data sets can be used. Weighting coefficients w_k^e help eliminate elements without strain measurement. Moreover, they serve to prioritize specific independent strain measures if required. For the inverse element utilized in this study, the least-squares functional defined in Equation (4) can be written as

$$\Phi(\boldsymbol{u}) = \sum_{\alpha=1}^{8} w_\alpha\, \varphi_\alpha, \tag{6}$$

where φ_α is defined as

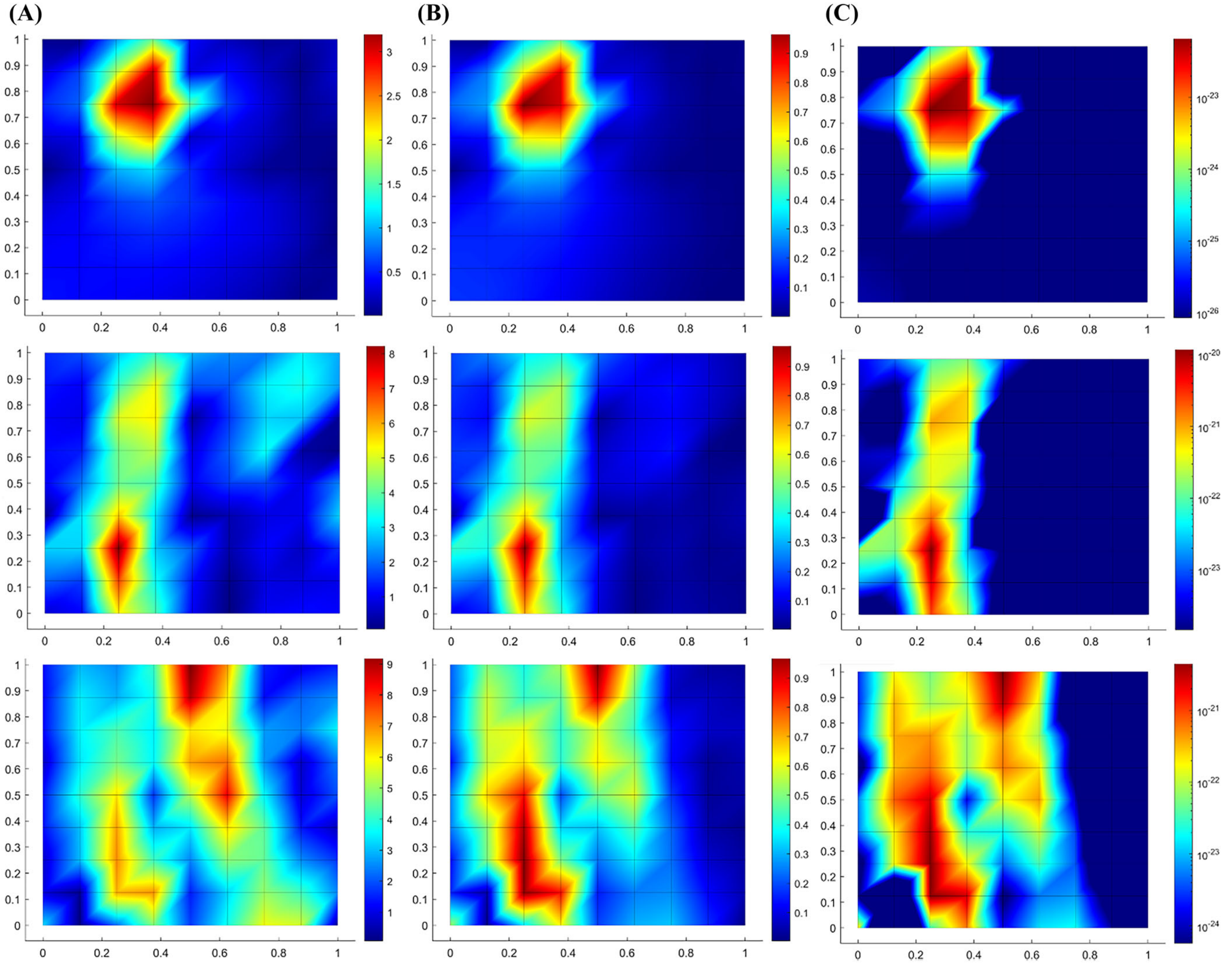

FIGURE 10 | Bending loading case for 8 × 8 sensors and mesh configuration by considering 10% thickness reduction. (A) PDP, (B) RDP, and (C) LDP from top row to bottom row for Case 1, Case 2, and Case 3. LDP, logarithmic damage parameter; PDP, percentage damage parameter; RDP, relative damage parameter.

$$\varphi_\alpha \equiv \frac{1}{n}\sum_{i=1}^{n}\left| e_\alpha(\boldsymbol{u})_i - E_{\alpha i}\right|^2 \quad (\alpha = 1, 2, 3), \tag{7}$$

$$\varphi_\alpha \equiv \frac{(2h)^2}{n}\sum_{i=1}^{n}\left|\kappa_\alpha(\boldsymbol{u})_i - K_{\alpha i}\right|^2 \quad (\alpha = 4, 5, 6), \tag{8}$$

$$\varphi_\alpha \equiv \frac{1}{n}\sum_{i=1}^{n}\left|g_\alpha(\boldsymbol{u})_i - G_{\alpha i}\right|^2 \quad (w_\alpha = \lambda) \quad (\alpha = 7, 8). \tag{9}$$

Additionally, in the case of unavailability of a measured strain component for a particular element, the equations will be reduced to L_2 squared norms of only analytical section strains as

$$\varphi_\alpha \equiv \tfrac{1}{A}\int_A \left|e_\alpha(\boldsymbol{u})\right|^2 \, \mathrm{d}A \quad (w_\alpha = \lambda) \quad (\alpha = 1, 2, 3), \tag{10}$$

$$\varphi_\alpha \equiv \tfrac{(2h)^2}{A}\int_A \left|\kappa_\alpha(\boldsymbol{u})\right|^2 \, \mathrm{d}A \quad (w_\alpha = \lambda) \quad (\alpha = 4, 5, 6), \tag{11}$$

$$\varphi_\alpha \equiv \frac{1}{A}\int_A \left|g_\alpha(\boldsymbol{u})\right|^2 \, \mathrm{d}A \quad (w_\alpha = \lambda) \quad (\alpha = 7, 8), \tag{12}$$

where the weighting coefficients are specified to be a negligibly small number, for example, $\lambda = 10^{-5}$.

2.3 | Analytical Strains and Inverse Element Formulation

In this study, iQS4 quadrilateral inverse element [14], which has six DOFs at each node (see Figure 2) and adopts the kinematics of the first-order shear deformation theory (FSDT), is utilized. In compliance with the FSDT, u_x, u_y, and u_z representing the orthogonal components of the displacement vector for any point across the shell is defined as

$$\begin{aligned} u_x(x, y, z) &= u(x, y) + z\theta_y(x, y), \\ u_y(x, y, z) &= v(x, y) - z\theta_x(x, y), \\ u_z(x, y, z) &= w(x, y), \end{aligned} \tag{13}$$

where u, v, w, θ_x, and θ_y are the midplane translational displacements and rotational components.

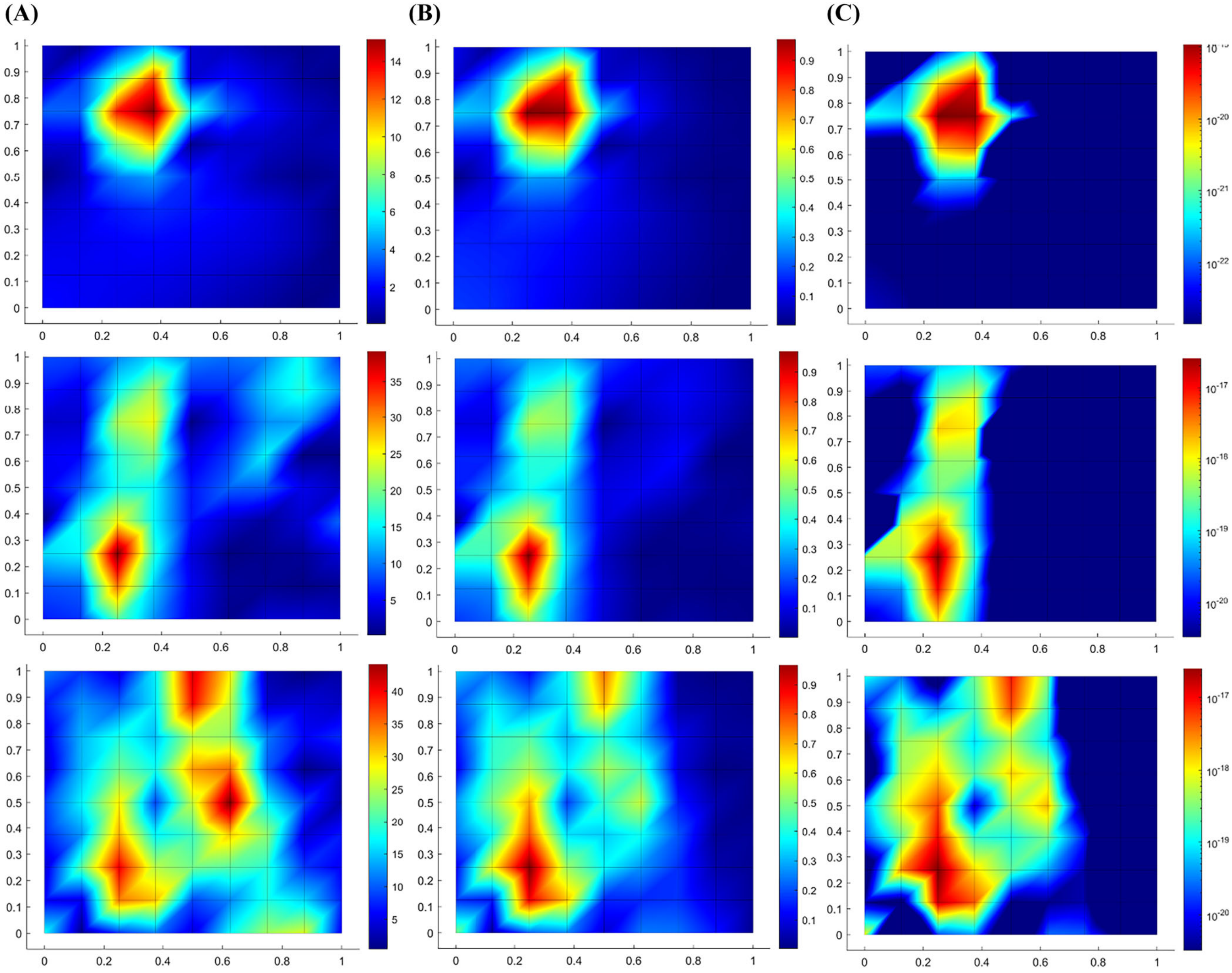

FIGURE 11 | Bending loading case for 8 × 8 sensors and mesh configuration by considering 40% thickness reduction. (A) PDP, (B) RDP, and (C) LDP from top row to bottom row for Case 1, Case 2, and Case 3. LDP, logarithmic damage parameter; PDP, percentage damage parameter; RDP, relative damage parameter.

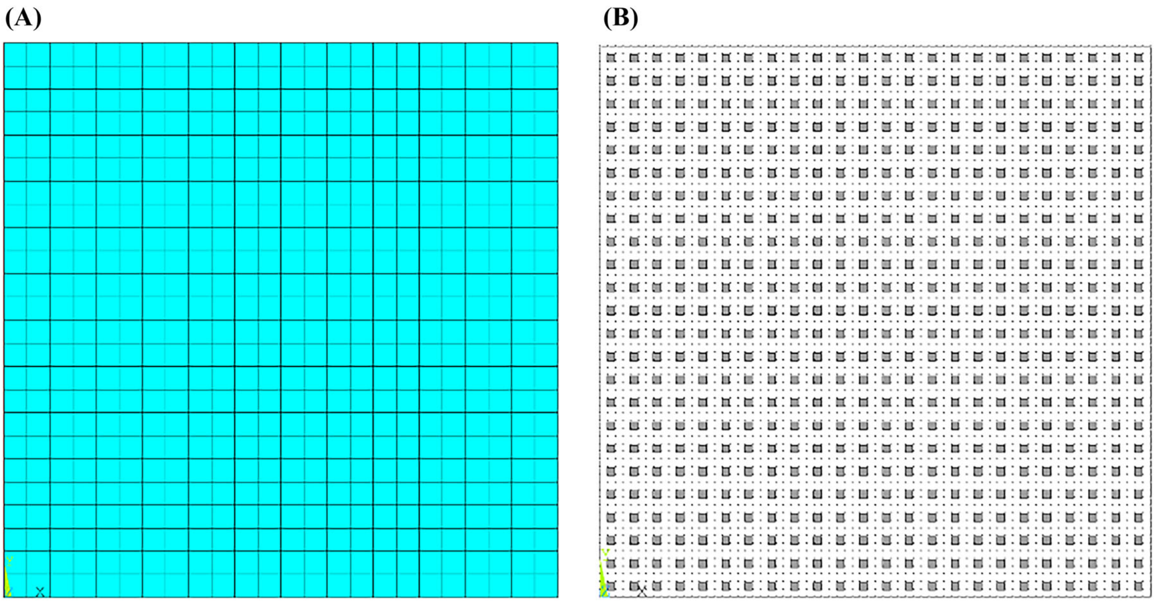

FIGURE 12 | (A) iFEM mesh with 24 × 24 elements and (B) 24 × 24 sensors for the iFEM model. iFEM, inverse finite element method.

Analytical section strains are calculated by using the derivatives of kinematic variables of iQS4, which are explicitly given by Kefal et al. [14]. The resulting forms of the analytical section strains are given as

$$\boldsymbol{e}(\boldsymbol{u}^{\mathrm{e}}) = [\boldsymbol{B}_1\boldsymbol{u}^{\mathrm{e}} \quad \boldsymbol{B}_2\boldsymbol{u}^{\mathrm{e}} \quad \boldsymbol{B}_3\boldsymbol{u}^{\mathrm{e}}]^{\mathrm{T}}, \tag{14}$$

$$\boldsymbol{\varkappa}(\boldsymbol{u}^{\mathrm{e}}) = [\boldsymbol{B}_4\boldsymbol{u}^{\mathrm{e}} \quad \boldsymbol{B}_5\boldsymbol{u}^{\mathrm{e}} \quad \boldsymbol{B}_6\boldsymbol{u}^{\mathrm{e}}]^{\mathrm{T}}, \tag{15}$$

$$\boldsymbol{g}(\boldsymbol{u}^{\mathrm{e}}) = [\boldsymbol{B}_7\boldsymbol{u}^{\mathrm{e}} \quad \boldsymbol{B}_8\boldsymbol{u}^{\mathrm{e}}]^{\mathrm{T}}, \tag{16}$$

where the displacement vector $\boldsymbol{u}^{\mathrm{e}}$ contains the nodal displacement values of the element, and the matrices $\boldsymbol{B}_\alpha$ ($\alpha = 1 \cdots 8$) contain derivatives of the relevant shape functions.

Once the strain values are calculated by using Equations (1) and (2), the weighted least-squares functional, which is given in Equation (5), can be written as

$$\begin{aligned}\Phi_{\mathrm{e}}(\boldsymbol{u}) = \frac{1}{n}\sum_{i=1}^{n}\Bigg(&\sum_{\alpha=1}^{3} w_\alpha |e_a(\boldsymbol{u}^{\mathrm{e}})_i - E_{ai}|^2 + (2h)^2\sum_{\alpha=4}^{6} w_\alpha \\ &|k_a(\boldsymbol{u}^{\mathrm{e}})_i - K_{ai}|^2 + \sum_{a=7}^{8} w_\alpha |g_\alpha(\boldsymbol{u})_i - G_{ai}|^2\Bigg).\end{aligned} \tag{17}$$

All strain compatibility relationships are explicitly satisfied based on these assumptions. Therefore, Equation (5) can be minimized with respect to displacement vector $\boldsymbol{u}$ as

$$\begin{aligned}\frac{\partial\Phi_{\mathrm{e}}(\boldsymbol{u}^{\mathrm{e}})}{\partial\boldsymbol{u}^{\mathrm{e}}} = \frac{1}{n}\sum_{i=1}^{n}\Bigg(&\sum_{\alpha=1}^{3} w_\alpha \frac{\partial|e_a(\boldsymbol{u}^{\mathrm{e}})_i - E_{ai}|^2}{\partial\boldsymbol{u}^{\mathrm{e}}} \\ &+ (2h)^2\sum_{\alpha=4}^{6} w_\alpha \frac{\partial|\kappa_\alpha(\boldsymbol{u}^{\mathrm{e}})_i - K_{ai}|^2}{\partial\boldsymbol{u}^{\mathrm{e}}} \\ &+ \sum_{\alpha=7}^{8} w_\alpha \frac{\partial|g_a(\boldsymbol{u}^{\mathrm{e}})_i - G_{ai}|^2}{\partial\boldsymbol{u}^{\mathrm{e}}}\Bigg) = 0.\end{aligned} \tag{18}$$

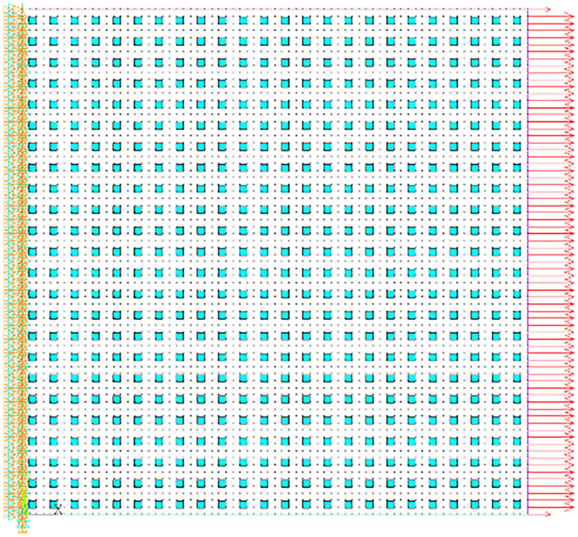

FIGURE 13 | A 24 × 24 sensor configuration and the distributed in-plane loading of 10 kN on the right edge.

By substituting Equations (14)–(16), Equation (18) can be rewritten as

$$\frac{\partial\,|\,e_a(\boldsymbol{u}^{\mathrm{e}})_i - E_{ai}|^2}{\partial\boldsymbol{u}^{\mathrm{e}}} = 2[\boldsymbol{B}_a(\boldsymbol{x}_i)\boldsymbol{u}^{\mathrm{e}} - E_{ai}]^{\mathrm{T}}\boldsymbol{B}_a(\boldsymbol{x}_i) \quad (\alpha = 1, 2, 3), \tag{19}$$

$$\frac{\partial\,|\,\kappa_\alpha(\boldsymbol{u}^{\mathrm{e}})_i - K_{ai}|^2}{\partial\boldsymbol{u}^{\mathrm{e}}} = 2[\boldsymbol{B}_a(\boldsymbol{x}_i)\boldsymbol{u}^{\mathrm{e}} - K_{ai}]^{\mathrm{T}}\boldsymbol{B}_a(\boldsymbol{x}_i) \quad (\alpha = 4, 5, 6), \tag{20}$$

$$\frac{\partial\,|\,e_a(\boldsymbol{u}^{\mathrm{e}})_i - G_{ai}|^2}{\partial\boldsymbol{u}^{\mathrm{e}}} = 2[\boldsymbol{B}_a(\boldsymbol{x}_i)\boldsymbol{u}^{\mathrm{e}} - G_{ai}]^{\mathrm{T}}\boldsymbol{B}_a(\boldsymbol{x}_i) \quad (\alpha = 7, 8), \tag{21}$$

$$\frac{\partial\Phi_{\mathrm{e}}(\boldsymbol{u}^{\mathrm{e}})}{\partial\boldsymbol{u}^{\mathrm{e}}} = 2(\boldsymbol{K}^{\mathrm{e}}\boldsymbol{u}^{\mathrm{e}} - \boldsymbol{\varepsilon}^{\mathrm{e}}) = 0, \tag{22}$$

$$\boldsymbol{K}^{\mathrm{e}}\boldsymbol{u}^{\mathrm{e}} = \boldsymbol{\varepsilon}^{\mathrm{e}}, \tag{23}$$

where $\boldsymbol{K}^{\mathrm{e}}$ and $\boldsymbol{\varepsilon}^{\mathrm{e}}$ are the left-hand-side matrix and strain vector for an iQS4 element, which can explicitly be calculated as

$$\begin{aligned}\boldsymbol{K}^{\mathrm{e}} = \frac{1}{n}\sum_{1}^{n}\Bigg(&\sum_{a=1}^{3}[w_a[\boldsymbol{B}_a(\boldsymbol{x}_i)]^{\mathrm{T}}\boldsymbol{B}_a(\boldsymbol{x}_i)]\\ &+(2h)^2\sum_{a=4}^{6}[w_a[\boldsymbol{B}_a(\boldsymbol{x}_i)]^{\mathrm{T}}\boldsymbol{B}_a(\boldsymbol{x}_i)] + \sum_{a=7}^{8}[w_a[\boldsymbol{B}_a(\boldsymbol{x}_i)]^{\mathrm{T}}\boldsymbol{B}_a(\boldsymbol{x}_i)]\Bigg),\end{aligned} \tag{24}$$

$$\begin{aligned}\boldsymbol{\varepsilon}^{\mathrm{e}} = \frac{1}{n}\sum_{1}^{n}\Bigg(&\sum_{a=1}^{3}[w_a[\boldsymbol{B}_a(\boldsymbol{x}_i)]^{\mathrm{T}}E_{ai}] + (2h)^2\sum_{a=4}^{6}[w_a[\boldsymbol{B}_a(\boldsymbol{x}_i)]^{\mathrm{T}}K_{ai}]\\ &+\sum_{a=7}^{8}[w_a[\boldsymbol{B}_a(\boldsymbol{x}_i)]^{\mathrm{T}}G_{ai}]\Bigg).\end{aligned} \tag{25}$$

The displacement vector $\boldsymbol{u}^{\mathrm{e}}$ can be obtained by solving the matrix system in Equation (23). Analytical section strains can then be calculated by using Equation (14).

2.4 | iFEM Corrosion Detection Procedure

The damage detection procedure begins by obtaining strain data from the intact structure. Then, the iFEM analysis is conducted to obtain full-field Von Mises strains ($\varepsilon_{\mathrm{vm,undamaged}}$) for the intact structure. Subsequently, strains are collected from the structure for the current state and iFEM analysis is conducted to determine the current Von Mises strains ($\varepsilon_{\mathrm{vm,current}}$). Having both sets of strains obtained, the damage parameter for the entire structure can be calculated, providing crucial insights into the structural health and identifying any areas of concern that may require further assessment or maintenance. This systematic approach enables effective monitoring and maintenance of structural integrity, ensuring safe and reliable operation over time. To achieve damage detection, full-field strain information

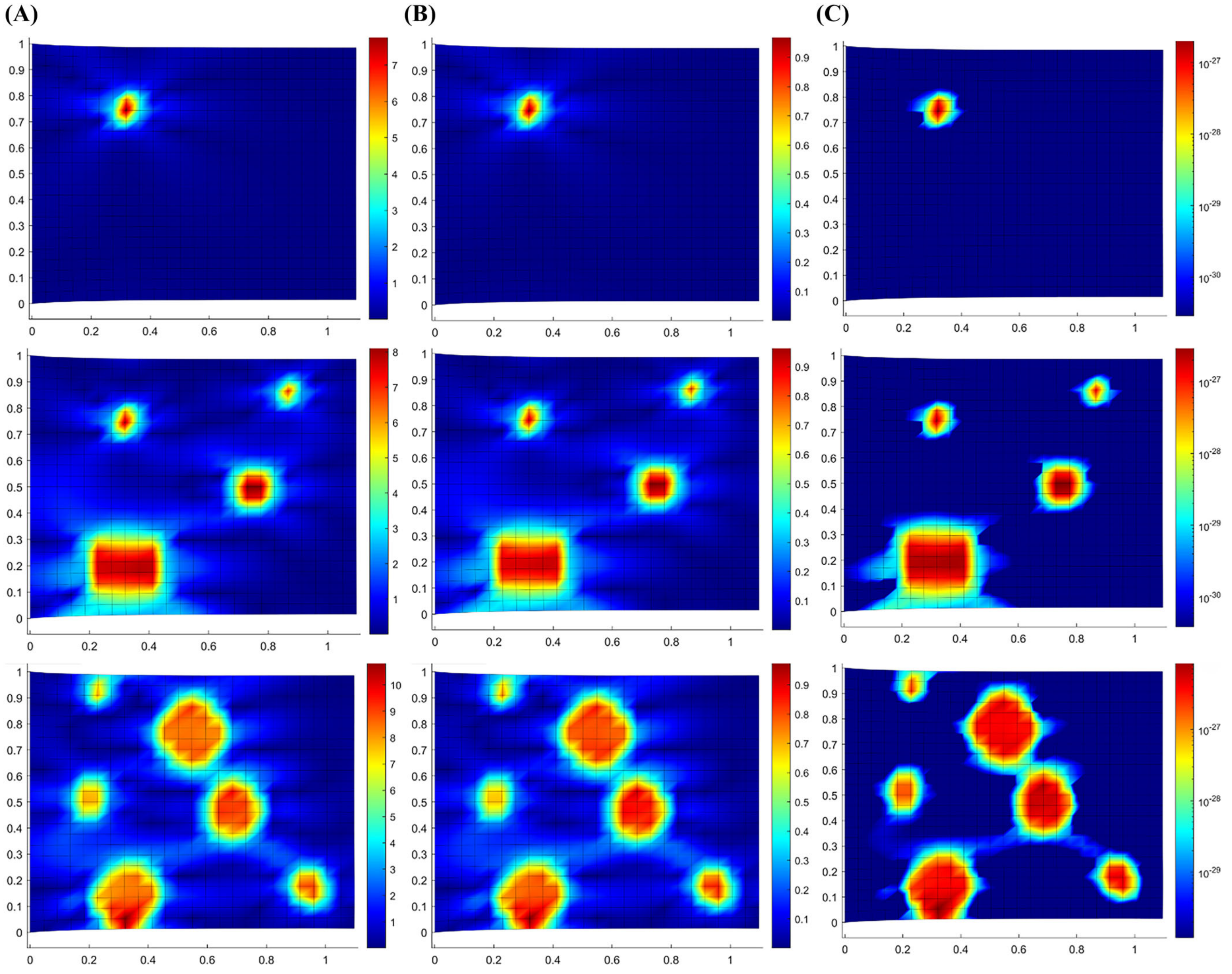

FIGURE 14 | Tension loading case for 24 × 24 sensors and mesh configuration by considering 10% thickness reduction. (A) PDP, (B) RDP, and (C) LDP from top row to bottom row for Case 1, Case 2, and Case 3. LDP, logarithmic damage parameter; PDP, percentage damage parameter; RDP, relative damage parameter.

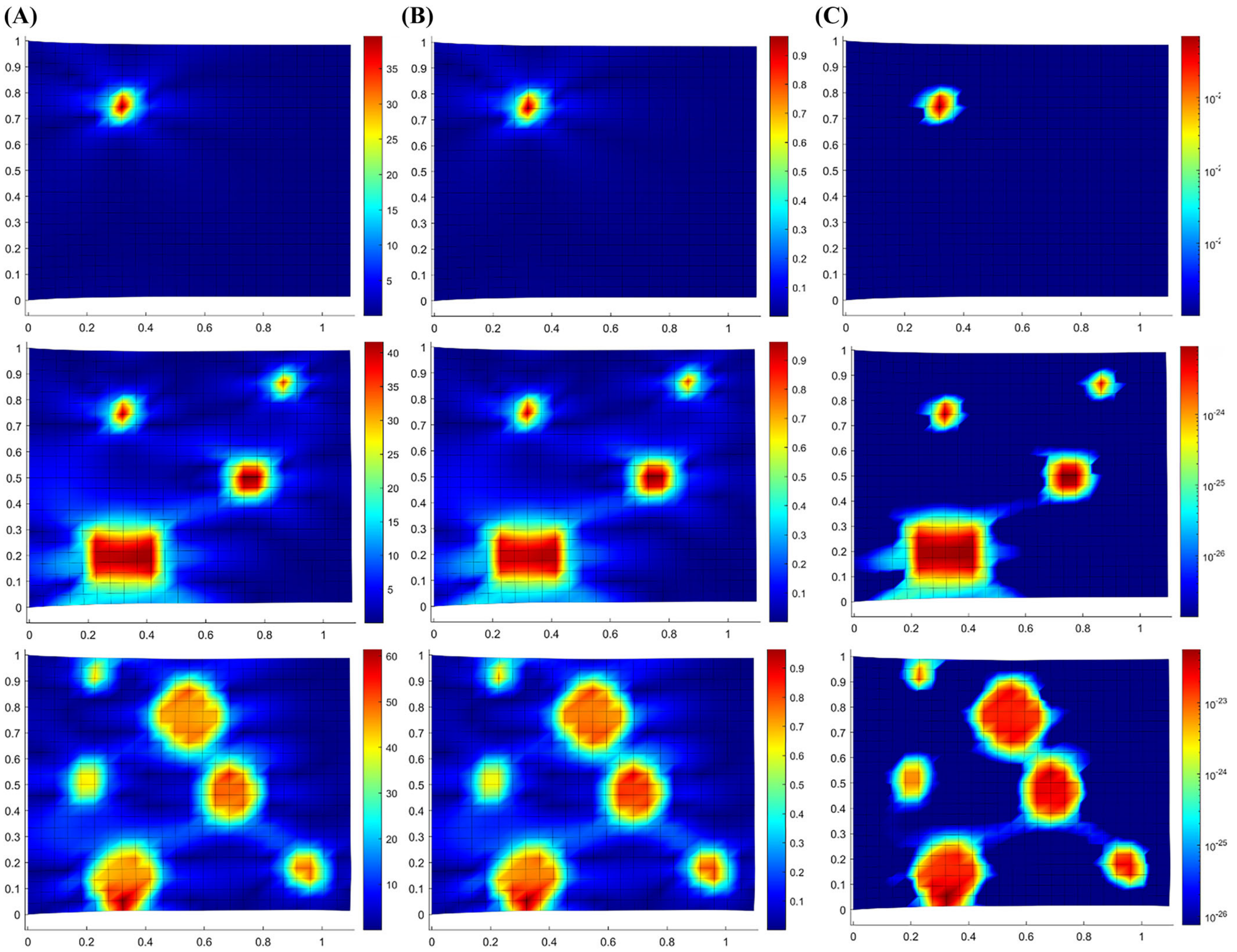

FIGURE 15 | Tension loading case for 24 × 24 sensors and mesh configuration by considering 40% thickness reduction. (A) PDP, (B) RDP, and (C) LDP from top row to bottom row for Case 1, Case 2, and Case 3. LDP, logarithmic damage parameter; PDP, percentage damage parameter; RDP, relative damage parameter.

is obtained by using the full-field displacement results achieved by performing the iFEM analysis of the structure.

In this study, three damage parameters are used for damage detection. The first one, which will be called as percentage damage parameter (PDP), was introduced by Li et al. [25] as

$$\mathrm{PDP} = \left| \frac{\varepsilon_{\mathrm{vm,current}} - \varepsilon_{\mathrm{vm,undamaged}}}{\varepsilon_{\mathrm{vm,undamaged}}} \right| \tag{26}$$

with Von Mises strain under plane-stress condition as

$$\varepsilon_{\mathrm{vm}} = \frac{1}{\sqrt{2}}\sqrt{(\varepsilon_{xx}-\varepsilon_{yy})^2+(\varepsilon_{xx}-\varepsilon_{zz})^2+(\varepsilon_{yy}-\varepsilon_{zz})^2+6\gamma_{xy}^2}, \tag{27}$$

$$\varepsilon_{zz} = \frac{\nu}{\nu-1}(\varepsilon_{xx}+\varepsilon_{yy}), \tag{28}$$

where ν is Poisson's ratio of the material.

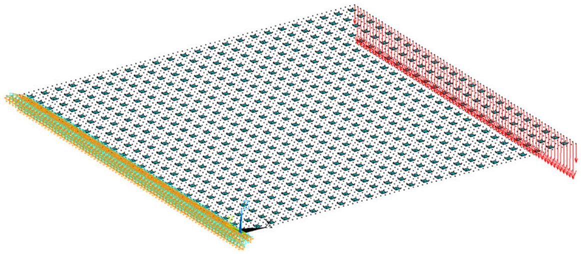

FIGURE 16 | A 24 × 24 sensor configuration and the distributed transverse loading of 1 kN on the right edge.

This method provides a damage index for each point on the target structure by performing an operation similar to calculation of absolute percentage individually for each node on the discretized numerical model. This method is quite effective to achieve an individual strain difference indicator for every part of the structure. However, when the strain difference becomes higher in small-strain locations than the one in high-strain locations, this parameter misses the criticality of the high-strain locations on the structure. For this reason, a relative damage parameter (RDP) is introduced in this paper by adopting PDP. It provides a damage index value which is calculated by utilizing the maximum strain values across the target structure to take into account the high-strain locations in the structure.

$$\mathrm{RDP} = \left| \frac{\varepsilon_{\mathrm{vm,current}} - \varepsilon_{\mathrm{vm,undamaged}}}{D_{\max}\, \varepsilon_{\mathrm{vm\ max,current}}} \right|, \tag{29}$$

where

$$D_{\max} = \left| \frac{\varepsilon_{\mathrm{vm\ max,current}} - \varepsilon_{\mathrm{vm,undamaged}}}{\varepsilon_{\mathrm{vm\ max,current}}} \right|. \tag{30}$$

This parameter provides results between 0 and 1 to detect the location of the damage.

Moreover, to achieve a more distinctive indication in contour values to assess the damage condition of the structure for high-strain locations, RDP is modified into logarithmic damage parameter (LDP) as

$$\mathrm{LDP} = \left| \frac{(\varepsilon_{\mathrm{vm,current}} - \varepsilon_{\mathrm{vm,undamaged}})^{a}}{D_{\max}\, \varepsilon_{\mathrm{vm\ max,current}}} \right|, \tag{31}$$

where a is chosen as 5 to generate sharper contour value differences in between the intact and damaged locations when the logarithmic scaling is preferred. To utilize the results achieved by using LDP effectively, the logarithmic scaling in contour plots should be used.

3 | Numerical Results

In this section, several numerical cases are considered to validate and demonstrate the capability of the current approach for corrosion damage detection. iFEM analysis is conducted without using actual experimentally acquired strain data. Instead, the strain data for iFEM is generated through FEM analysis as synthetic data as detailed in subsequent sections of the numerical examples.

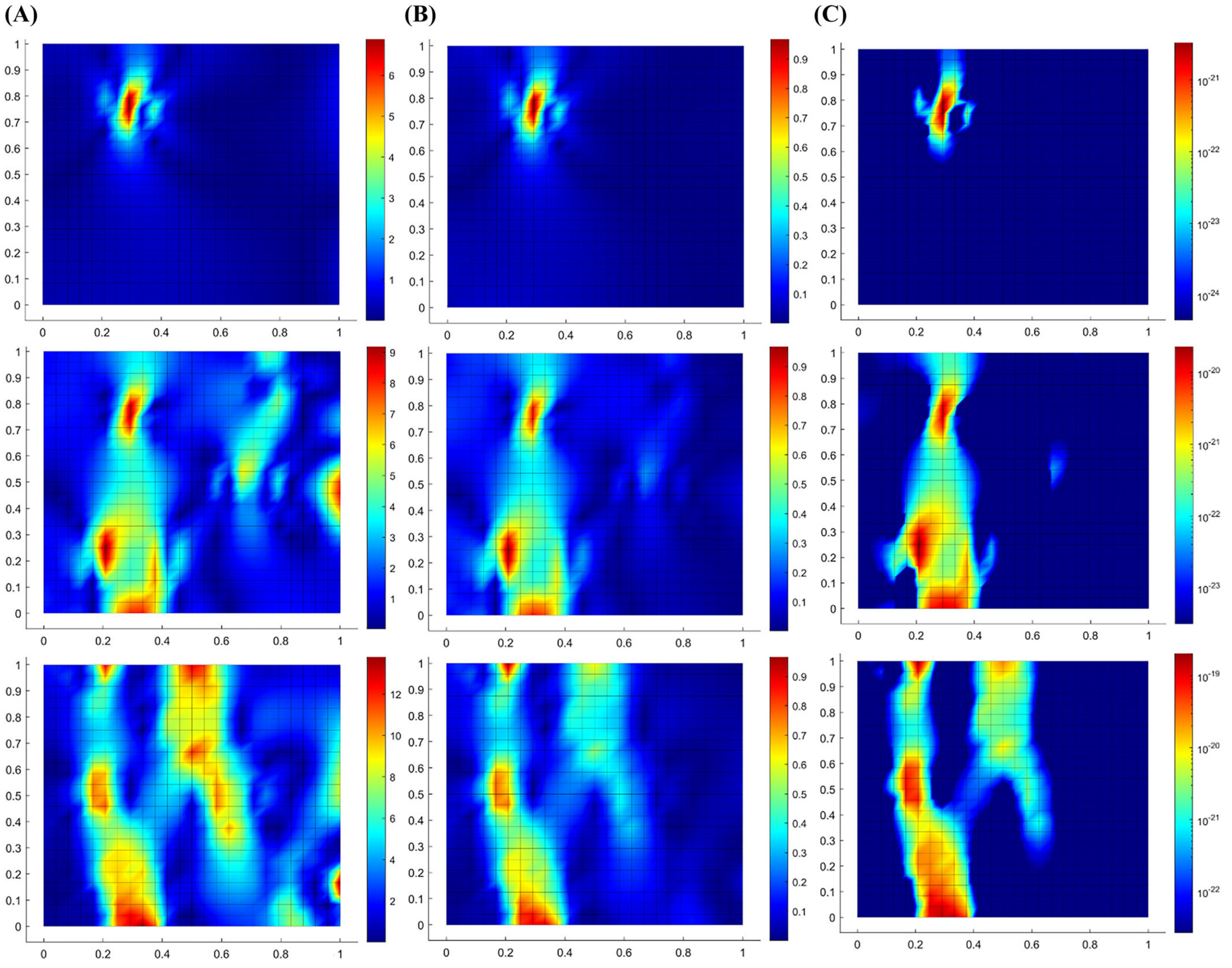

FIGURE 17 | Bending loading case for 24 × 24 sensors and mesh configuration by considering 10% thickness reduction. (A) PDP, (B) RDP, and (C) LDP from top row to bottom row for Case 1, Case 2, and Case 3. LDP, logarithmic damage parameter; PDP, percentage damage parameter; RDP, relative damage parameter.

3.1 | Square Plate

The performance of iFEM in corrosion damage prediction is demonstrated for a thin steel plate with dimensions of 1 m × 1 m × 0.01 m, subjected to cantilever boundary conditions. To make the assessment in two different loading scenarios, including tension and transverse bending, 10 kN distributed load in the positive x-direction and a 1-kN distributed load in the negative z-direction are applied to the free end. Three corrosion scenarios are examined, as shown in Figure 3, each with two thickness reduction levels: 10% and 40%. Moreover, two sensor configurations, including 8 × 8 (see Figure 5) and 24 × 24 (see Figure 12) sets of rosettes, are considered. iFEM element meshes are selected to demonstrate the effect of sensor density on the definition of damage detection results. Synthetic strain data were generated by using the FEM model shown in Figure 4.

3.1.1 | Coarse iFEM Mesh Scenario

In this first scenario, coarse iFEM mesh is considered, as depicted in Figure 5A. The corresponding 8 × 8 sensor configuration is given in Figure 5B. Note that there is one sensor corresponding to each iFEM element.

3.1.2 | Coarse iFEM Mesh Scenario—Tension Case

In the first numerical case, a tension loading of 10 kN is applied to the right edge, where the left edge is fully fixed, as shown in Figure 6. For the three corrosion damage cases given in Figure 3 and for two different thickness reduction scenarios, 10% and 40%, iFEM corrosion damage predictions are demonstrated in Figures 7 and 8 by using three damage parameters: PDP, RDP, and LDP, for damage detection. For both 10% and 40% thickness reduction scenarios, all three damage parameters, PDP, RDP, and LDP, yield similar corrosion damage predictions. For a single damage case, iFEM captures the correct damage location, whereas it has difficulty in detecting small damaged regions compared with the large damaged regions for multiple corrosion cases. This may be due to an insufficient number of sensors located on the structure.

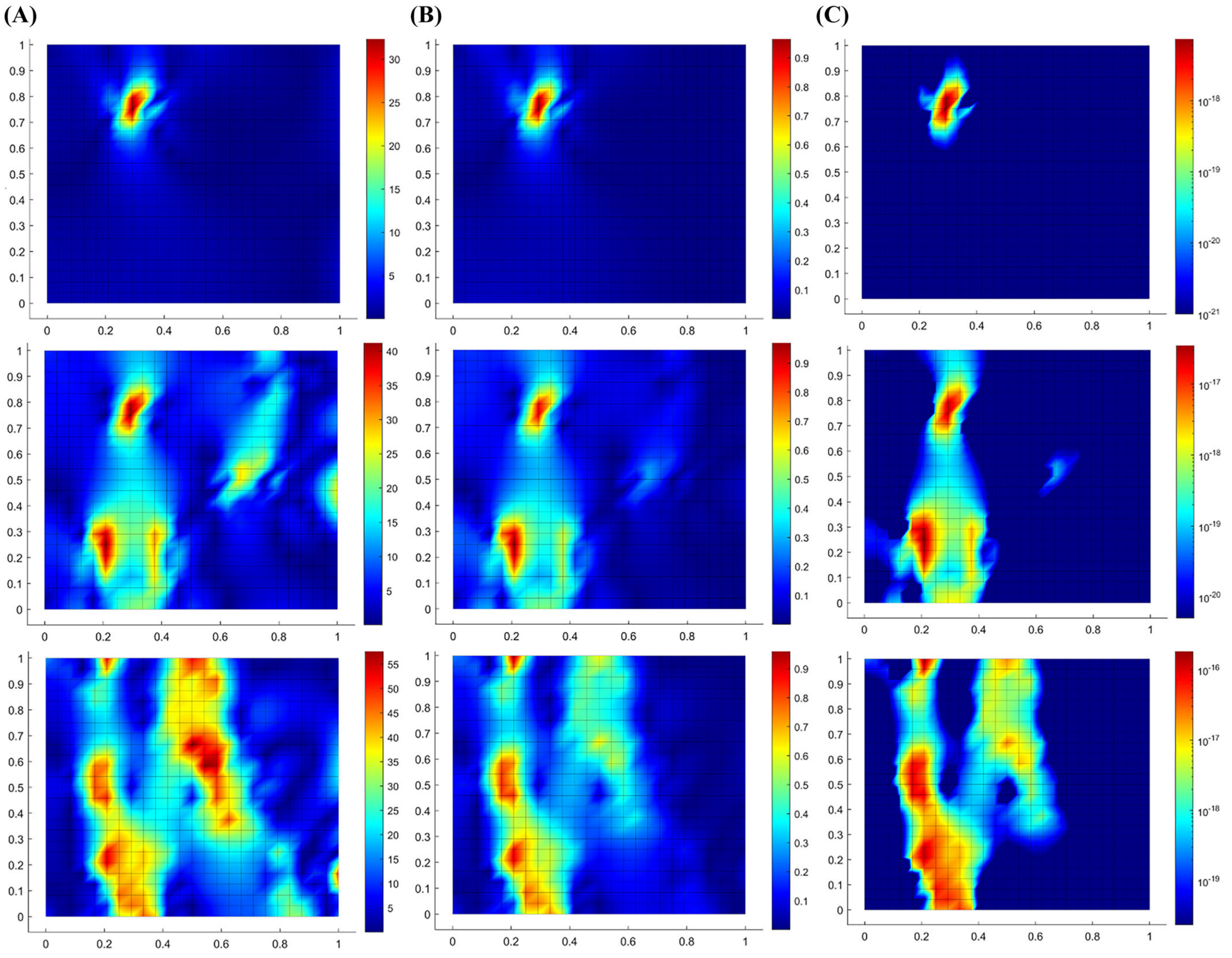

FIGURE 18 | Bending loading case for 24 × 24 sensors and mesh configuration by considering 40% thickness reduction. (A) PDP, (B) RDP, and (C) LDP from top row to bottom row for Case 1, Case 2, and Case 3. LDP, logarithmic damage parameter; PDP, percentage damage parameter; RDP, relative damage parameter.

3.1.3 | Coarse iFEM Mesh Scenario—Bending Case

In the second numerical case, bending loading of 1 kN is applied to the right edge, where the left edge is fully fixed, as shown in Figure 9. For two different thickness reduction scenarios, 10% and 40%, iFEM corrosion damage predictions are demonstrated in Figures 10 and 11 by using three damage parameters: PDP, RDP, and LDP, for damage detection. Similar to the tension loading results, iFEM captures the correct damage location for the single corrosion damage case for bending loading. However, for multiple damage cases, iFEM could not make reasonable damage predictions by considering an 8 × 8 sensor configuration.

3.1.4 | Fine iFEM Mesh Scenario

In this second scenario, finer iFEM mesh is considered, as depicted in Figure 12A. The corresponding 24 × 24 sensor

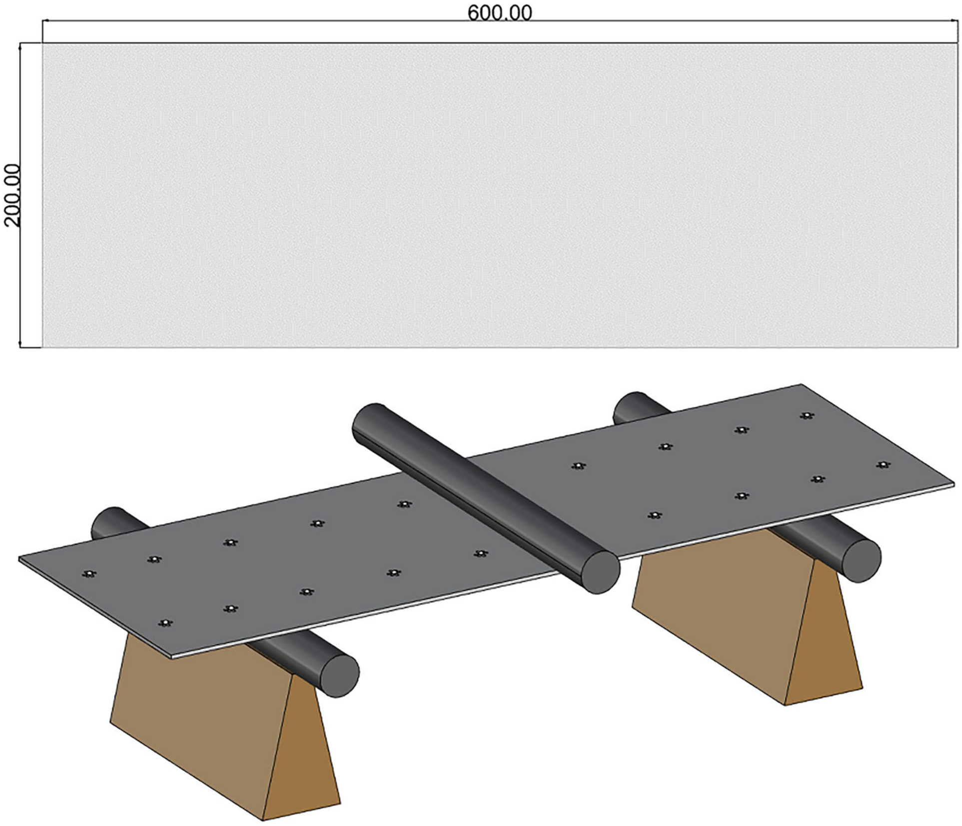

FIGURE 19 | Illustration of the plate dimensions and the three-point-bending scenario.

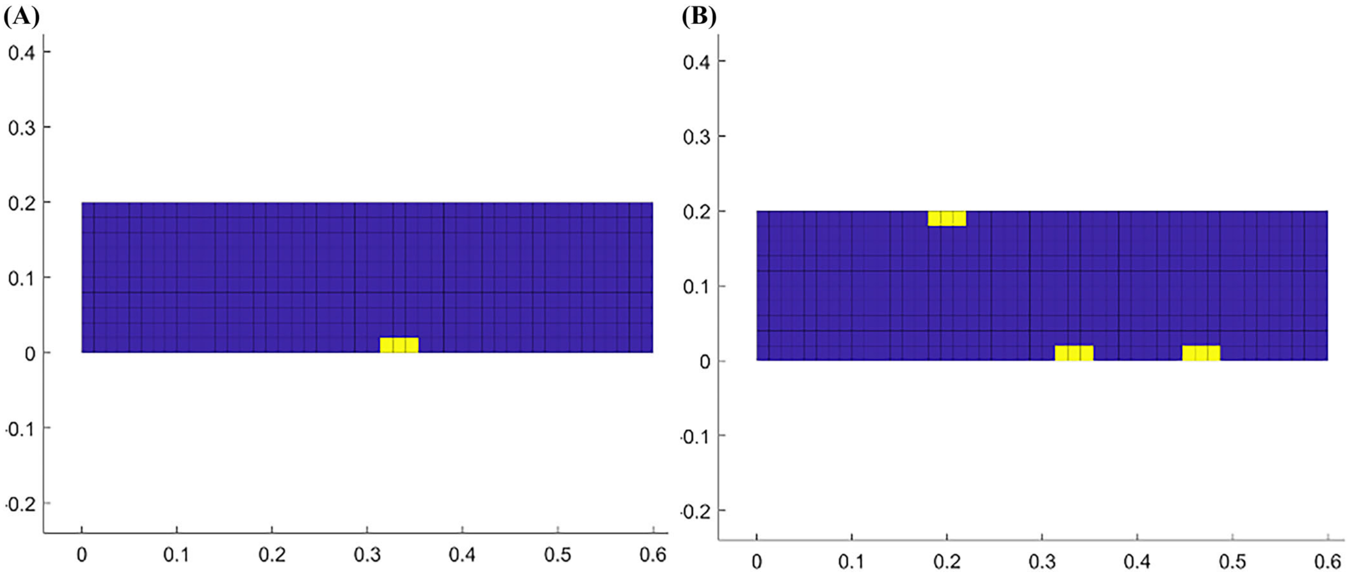

FIGURE 20 | Corrosion scenarios for a simple plate in three-point-bending test: (A) Case 1 and (B) Case 2.

configuration is given in Figure 12B. As in the coarse mesh case, there is one sensor corresponding to each iFEM element.

3.1.5 | Fine iFEM Mesh Scenario—Tension Case

In the first numerical case of the finer mesh scenario, a tension loading of 10 kN is applied to the right edge where the left edge is fully fixed, as shown in Figure 13. For two different thickness reduction scenarios, 10% and 40%, iFEM corrosion damage predictions are demonstrated in Figures 14 and 15 by using three damage parameters: PDP, RDP, and LDP, for damage detection. For all damage cases, a very good prediction outcome is achieved regardless of the damage parameter definition and the thickness ratio.

3.1.6 | Fine iFEM Mesh Scenario—Bending Case

In the second numerical case, bending loading of 1 kN is applied to the right edge, where the left edge is fully fixed, as shown in Figure 16. For two different thickness reduction

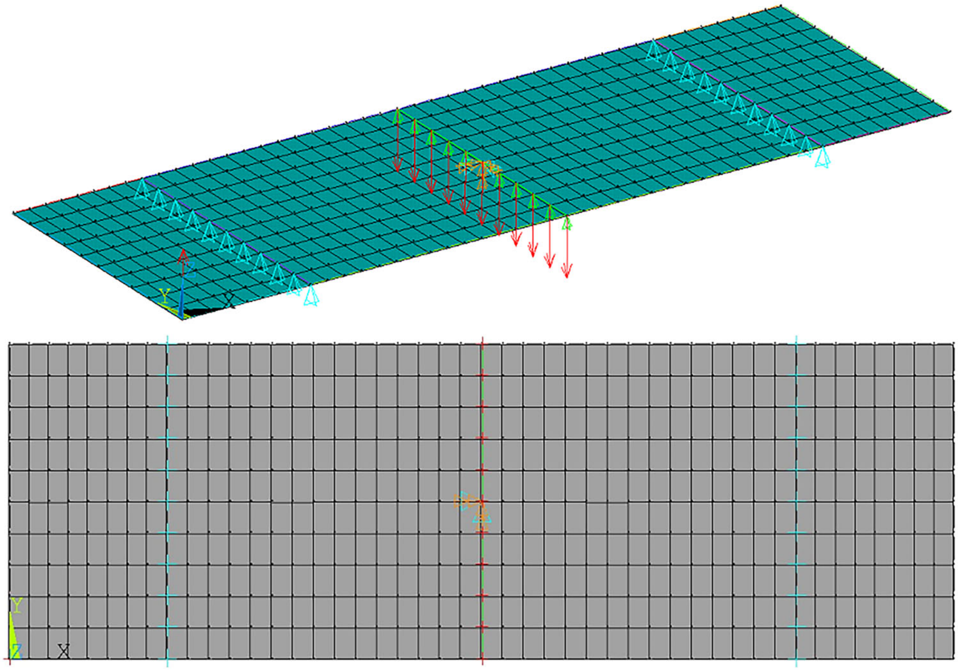

FIGURE 21 | FEM model with applied loading and defined boundary conditions for a simple plate in a three-point-bending test. FEM, finite element method.

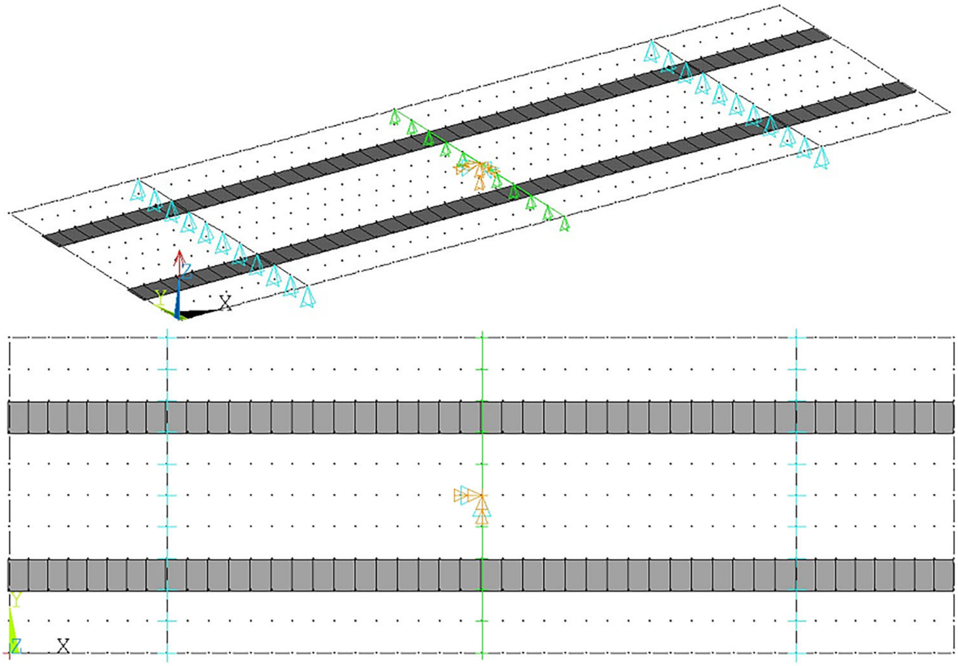

FIGURE 22 | Two-fine-array sensor configuration.

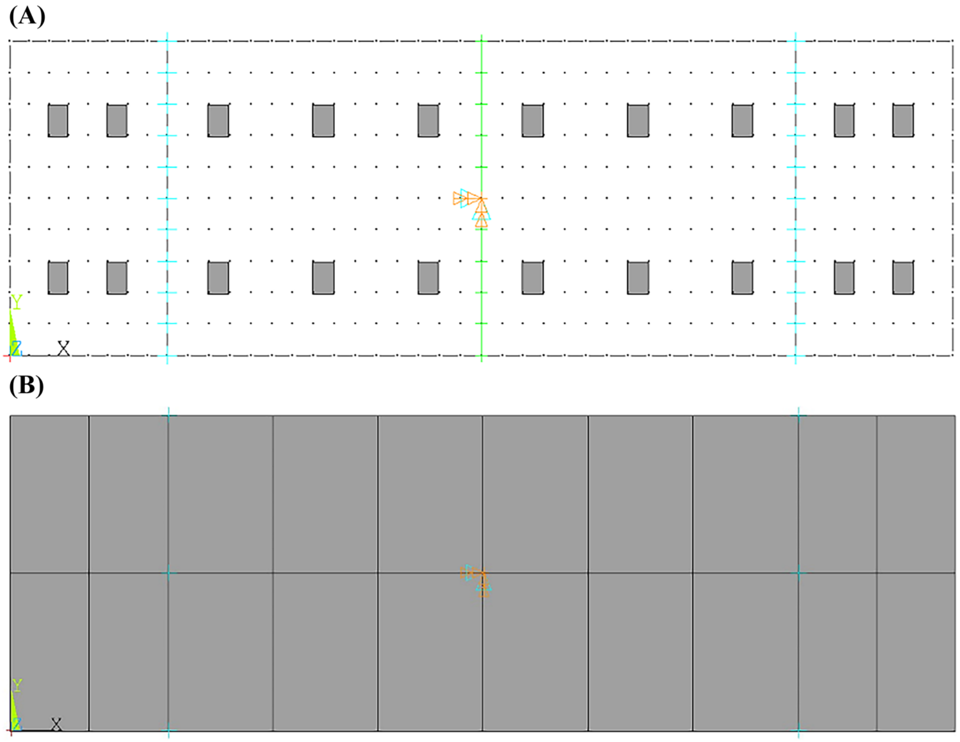

FIGURE 23 | Two-coarse-array sensor configuration (A) and coarse iFEM mesh (B). iFEM, inverse finite element method.

scenarios, 10% and 40%, iFEM corrosion damage predictions are demonstrated in Figures 17 and 18 by using three damage parameters: PDP, RDP, and LDP, for damage detection. For the single damage case, iFEM made a good prediction of the damage location. For the multiple damage cases, iFEM predictions gave a good indication of potential damage locations and are better with respect to the 8 × 8 coarse mesh case presented earlier.

Findings show that predicting corroded locations under bending scenarios is more challenging compared with tension scenarios, highlighting the complexity involved in such analyses.

3.2 | Simple Plate in Three-Point-Bending Test

In this section, in addition to the square model with relatively high number of strain sensors, to demonstrate the performance of iFEM on damage prediction along with practicality in terms of number of sensors, a new model is assessed by using various sensor configurations, which are explicitly defined in the following parts of the study. Since the effect of loading condition type on damage prediction is observed such that the transverse bending loading conditions cause more challenging damage prediction results, the loading condition is selected as three-point bending (see Figure 19) for this section of the study. A distributed 300 N of load is applied to the middle length of the structure, as shown in Figures 19 and 21. The dimensions of the specimen are 600 mm × 200 mm × 3 mm (see Figure 19), and it is made of 304 grade stainless steel.

Various damage scenarios with two thickness reduction cases, that is, 10% and 40% thickness reductions, are assessed for sensor installment cases of full sensor, fine array, and coarse array configurations.

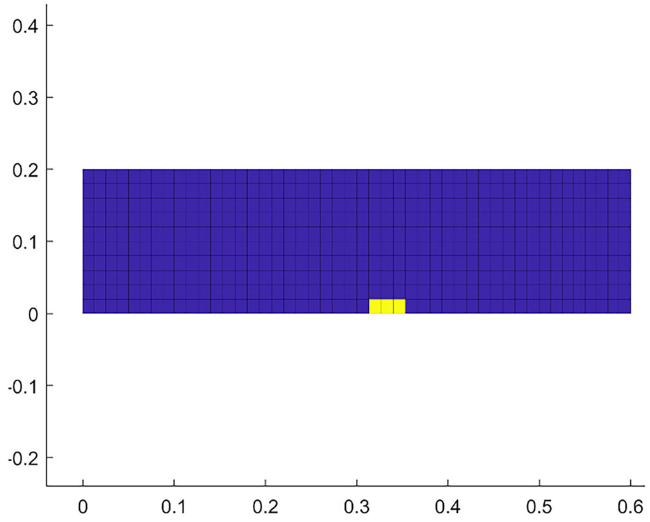

FIGURE 24 | Defined corrosion region for Case 1 on the target model.

Corrosion scenarios are selected (see Figure 20) to involve different numbers of multiple corroded patches on the target model to investigate the effect of locations of the corroded patches on the target structure in terms of damage prediction. Especially, the multiple damage cases provide important results to investigate the accuracy of iFEM and the used damage parameters on predicting corrosion locations in the presence of different levels of strain difference values on different locations of the damaged model in comparison with the

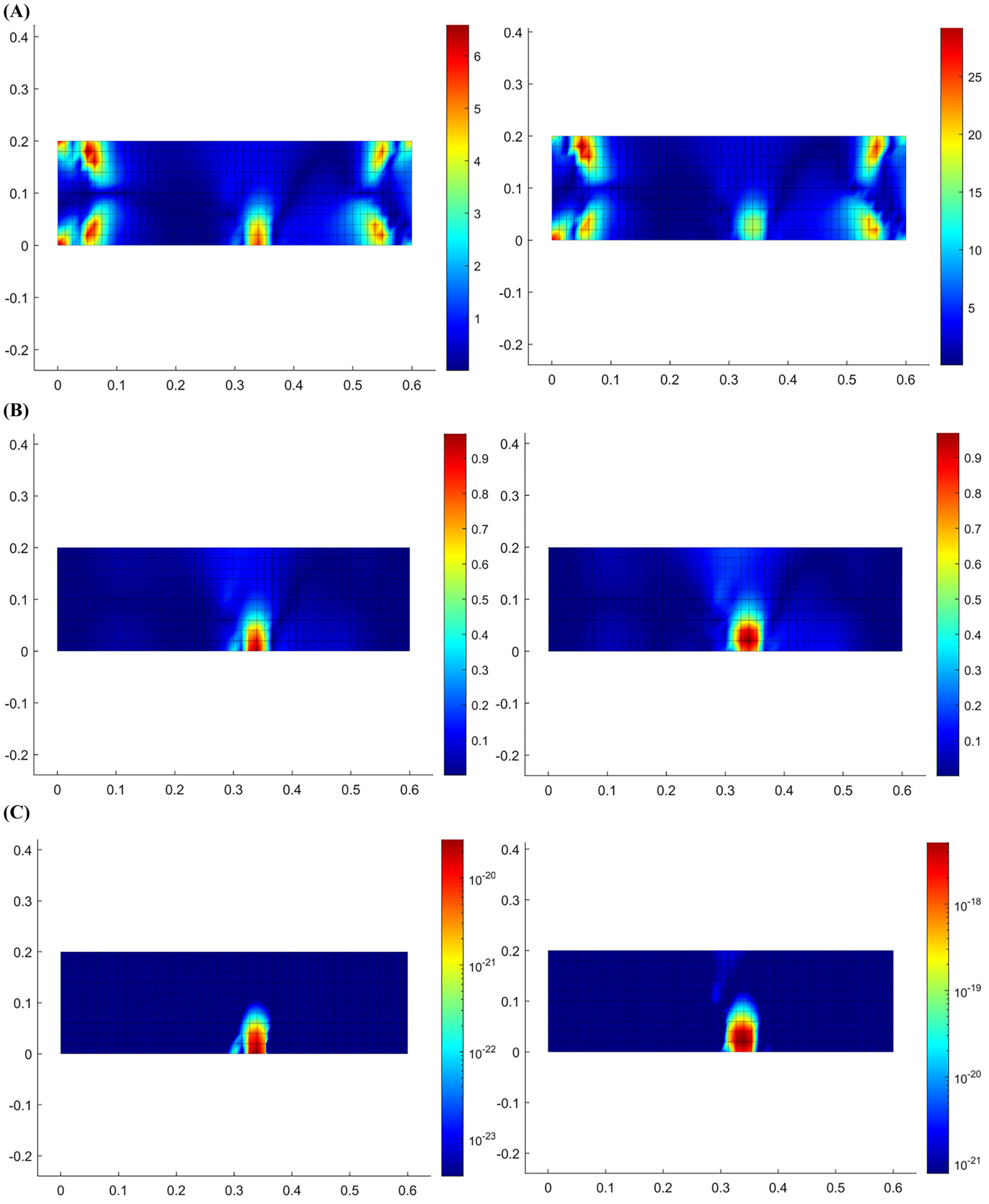

FIGURE 25 | Fine iFEM mesh—full sensor configuration by considering 10% (left column) and 40% (right column) thickness reduction. Row (A), row (B), and row (C) show PDP, RDP, and LDP, respectively. iFEM, inverse finite element method; LDP, logarithmic damage parameter; PDP, percentage damage parameter; RDP, relative damage parameter.

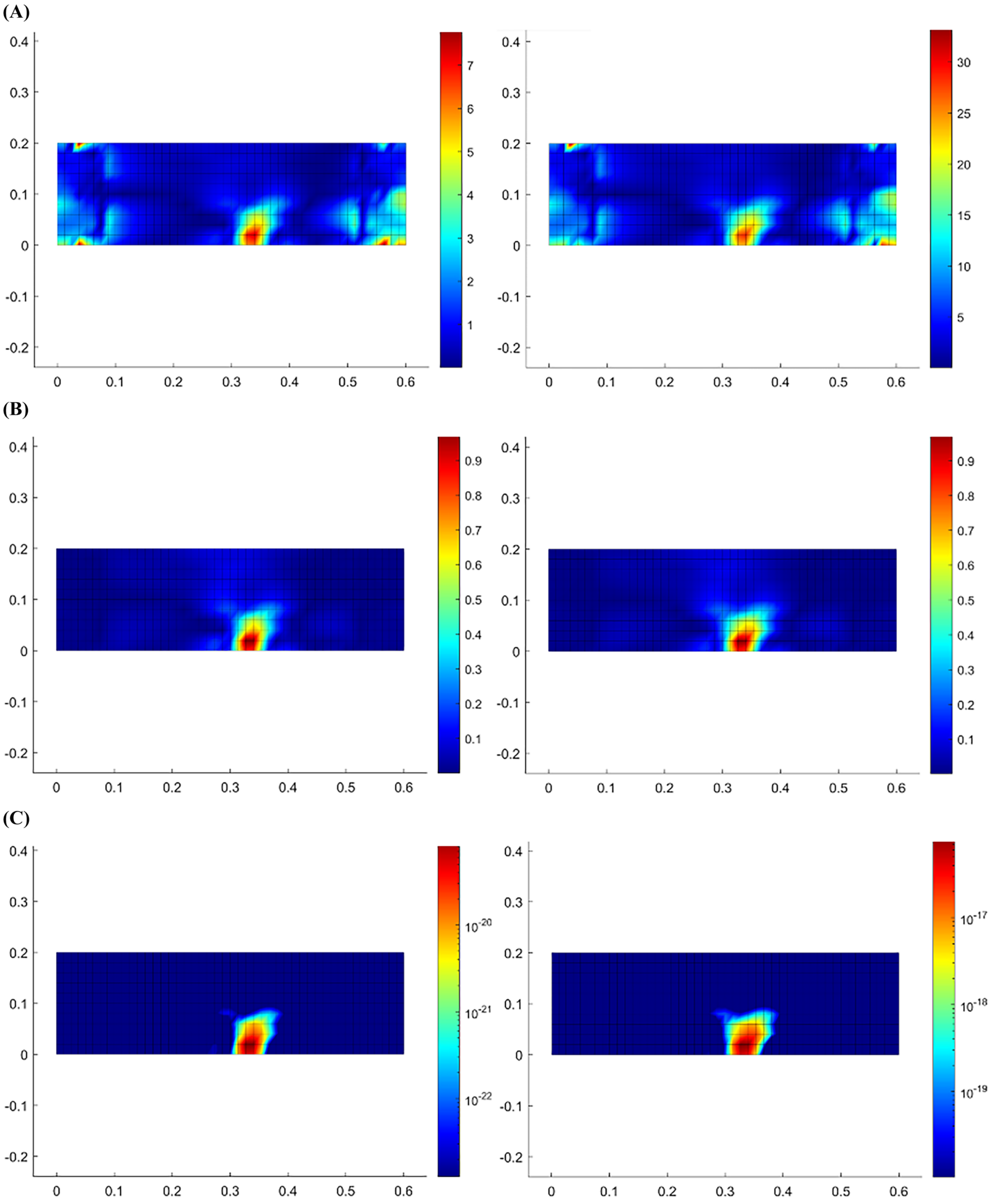

FIGURE 26 | Fine iFEM mesh—two-fine-arrays sensor configuration by considering 10% (left column) and 40% (right column) thickness reduction. Row (A), row (B), and row (C) show PDP, RDP, and LDP, respectively. iFEM, inverse finite element method; LDP, logarithmic damage parameter; PDP, percentage damage parameter; RDP, relative damage parameter.

intact structure. In some cases, high-strain differences in particular damaged portions of the structure may shadow the damages on relatively low-strain locations. In contrast to this, in some cases, strain percentage differences on intact low-strain locations may shadow the damages at high-strain locations. Therefore, the damage cases are selected to investigate the accuracy of different damage parameters and/or sensor configurations.

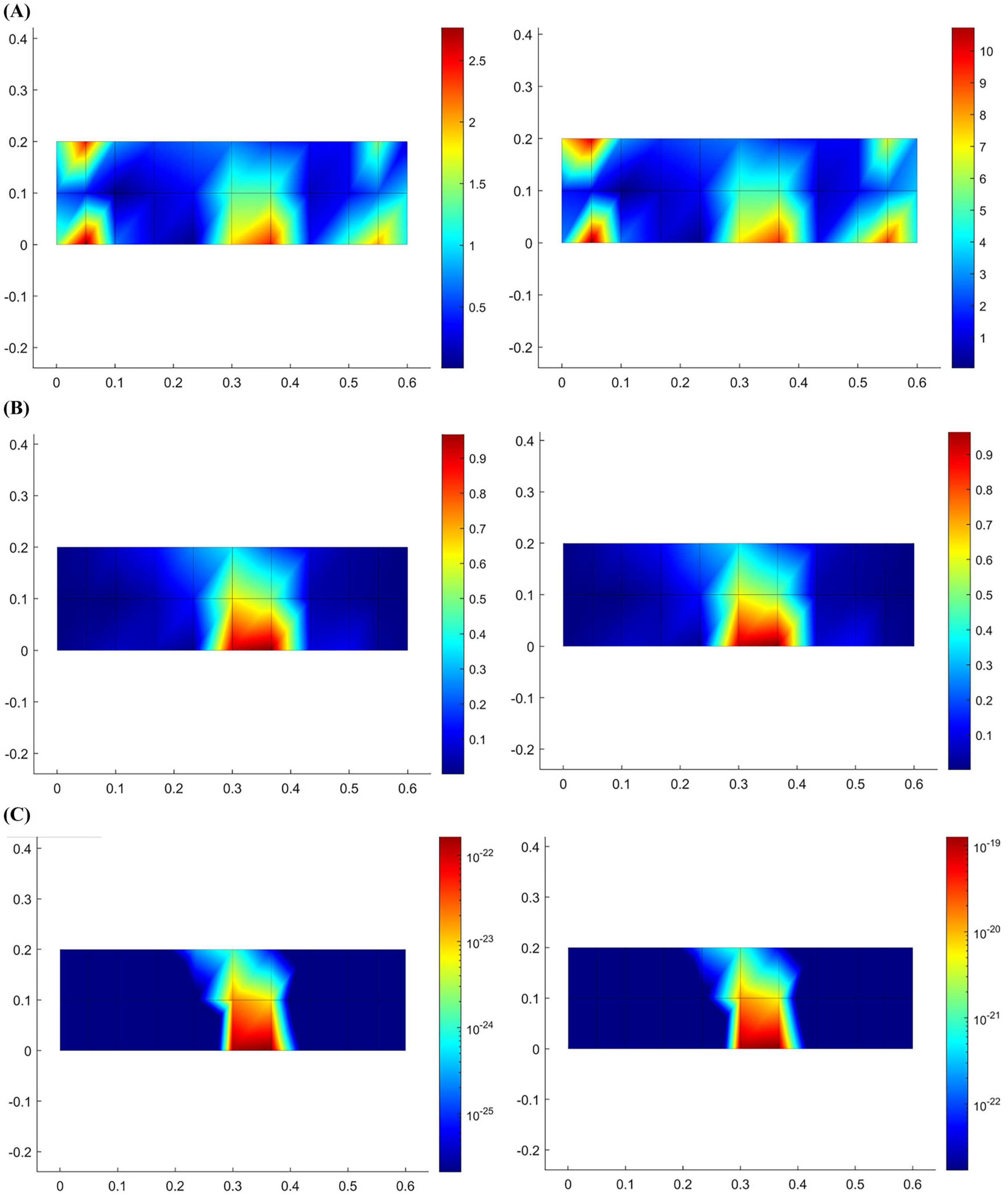

FIGURE 27 | Coarse iFEM mesh—two-coarse-arrays sensor configuration by considering 10% (left column) and 40% (right column) thickness reduction. Row (A), row (B), and row (C) show PDP, RDP, and LDP, respectively. iFEM, inverse finite element method; LDP, logarithmic damage parameter; PDP, percentage damage parameter; RDP, relative damage parameter.

PDP, RDP, and LDP damage parameter results are calculated for the defined corrosion scenarios in accordance with the following sensor configurations:

- full sensor configuration,
- fine array configuration,
- coarse array configuration.

For each sensor configuration, strain components ε_{11}, ε_{22}, and γ_{12} are gathered from the synthetic sensor locations on the FEM model.

In full sensor configuration fine FEM mesh (see Figure 21) is adopted the same as iFEM model such that all inverse elements are fed with strain data acquired from the FEM element counterpart. In this theoretical scenario, 460 iFEM elements are utilized to examine the conceptual performance of iFEM.

In fine array sensor configuration (see Figure 22), again the same fine mesh is utilized for the iFEM model with 460 inverse elements. However, this time, only two arrays are considered and 92 inverse elements along the structure are fed with synthetic strain data to assess a semi-practical SHM scenario. Please note that for those elements without strain measurement weighting coefficients are specified as a small value and the corresponding strain vector values are assigned as zero.

In the coarse array configuration (see Figure 23), a more realistic damage detection scenario is examined. In this configuration, a coarse mesh involving 20 elements is utilized for iFEM. In this scenario all of the 20 inverse elements are fed with the strain data collected from the synthetic strain sensor locations on the FEM model.

The difference in depth of the corrosion does not result in a significant difference in the damage detection performance of any of the damage parameters in any of the corrosion cases. However, in the presence of noise in the measured strain data, the effect of corrosion depth is expected to play a notable role.

3.2.1 | Single Corrosion Region at the Bottom Edge

This case investigates the damage prediction performance of the damage parameters for the given sensor configurations in the presence of a relatively small single corrosion patch (see Figure 24). The results indicate that RDP and LDP exhibit adequate performance in terms of accuracy of damage detection across all sensor configurations (see Figures 25–27). However, an important observation is that as the size of iFEM elements increases, the size of the predicted damage area tends to appear larger than the actual corroded patch size, potentially leading to an overestimation of the damage extent. PDP, on the other hand, is observed to capture the corroded patch, but tends to falsely indicate damage in the intact regions.

3.2.2 | Three Corrosion Regions at the Top and Bottom Edges

This case examines three corrosion regions at the top and bottom edges, as shown in Figure 28. As depicted in Figures 29–31, RDP and LDP damage parameters successfully detect the corroded regions between the supports. In contrast, PDP fails to identify the corroded areas and instead highlights the intact regions.

4 | Conclusions

In this study, iFEM is utilized for detecting corrosion damage in plates under different loading conditions, including tension and bending loadings. In addition to the PDP introduced by Li et al. [25], two new damage parameters RDP and LDP are introduced. Two different thickness reduction levels, that is, 10% and 40%, are considered first for a plate under tension or bending loading. Both coarse and fine mesh configurations are utilized. For the coarse mesh case, only the single damage case prediction was satisfactory, whereas multiple damage scenarios could not be well predicted. On the other hand, for the fine mesh case, all damage parameters performed very well for the tension loading and the single damage case for bending loading. However, for multiple damage cases, the same performance could not be achieved. To investigate this further, three-point-bending test was considered by introducing single and multiple damaged regions. On the basis of the majority of the results, it is observed that the newly introduced damage parameters RDP and LDP demonstrate good performance for predicting the location of the corrosion damage, whereas PDP does not perform well for most of the cases as the change in strain values in intact locations sometimes may occur higher than the damaged locations in percentage.

As a summary, the current study presented how iFEM can be utilized to monitor and detect corrosion damage by utilizing synthetic data and numerical examples. On the basis of the evaluated results, it was shown that iFEM has a very good

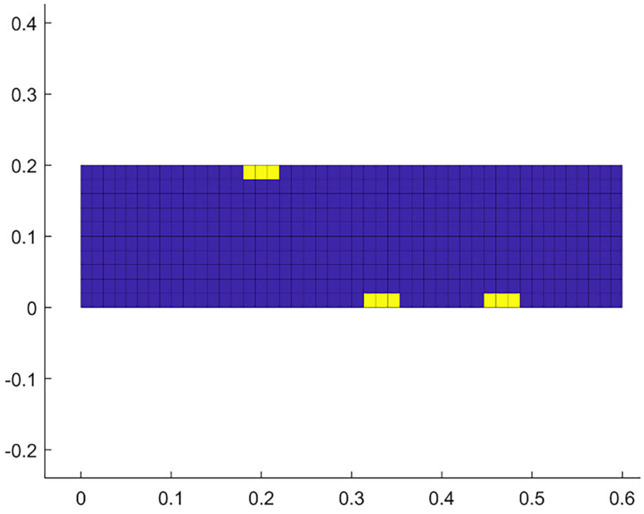

FIGURE 28 | Defined corrosion regions for Case 2 on the target model.

potential for this purpose and can be utilized for monitoring and detecting corrosion damage in real-world cases [26], which can be considered as a future study. Moreover, synthetic data can be utilized to determine the optimum sensor locations and required number of sensors. It is important to reduce the number of sensors due to practical reasons while satisfying sufficient accuracy. Therefore, once the optimization process is completed numerically by utilizing the synthetic data, sensors

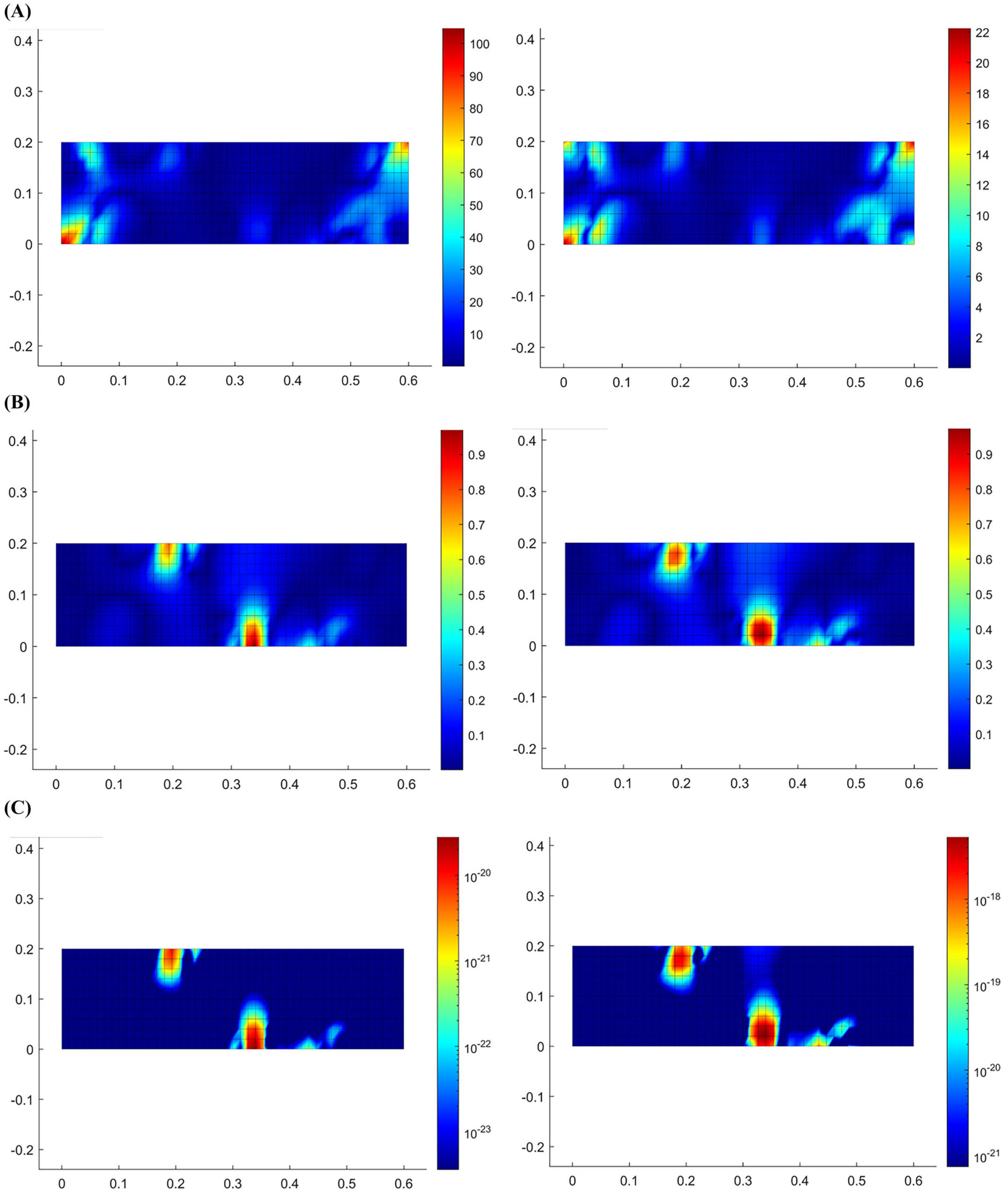

FIGURE 29 | Fine iFEM mesh—full sensor configuration by considering 10% (left column) and 40% (right column) thickness reduction. Row (A), row (B), and row (C) show PDP, RDP, and LDP, respectively. iFEM, inverse finite element method; LDP, logarithmic damage parameter; PDP, percentage damage parameter; RDP, relative damage parameter.

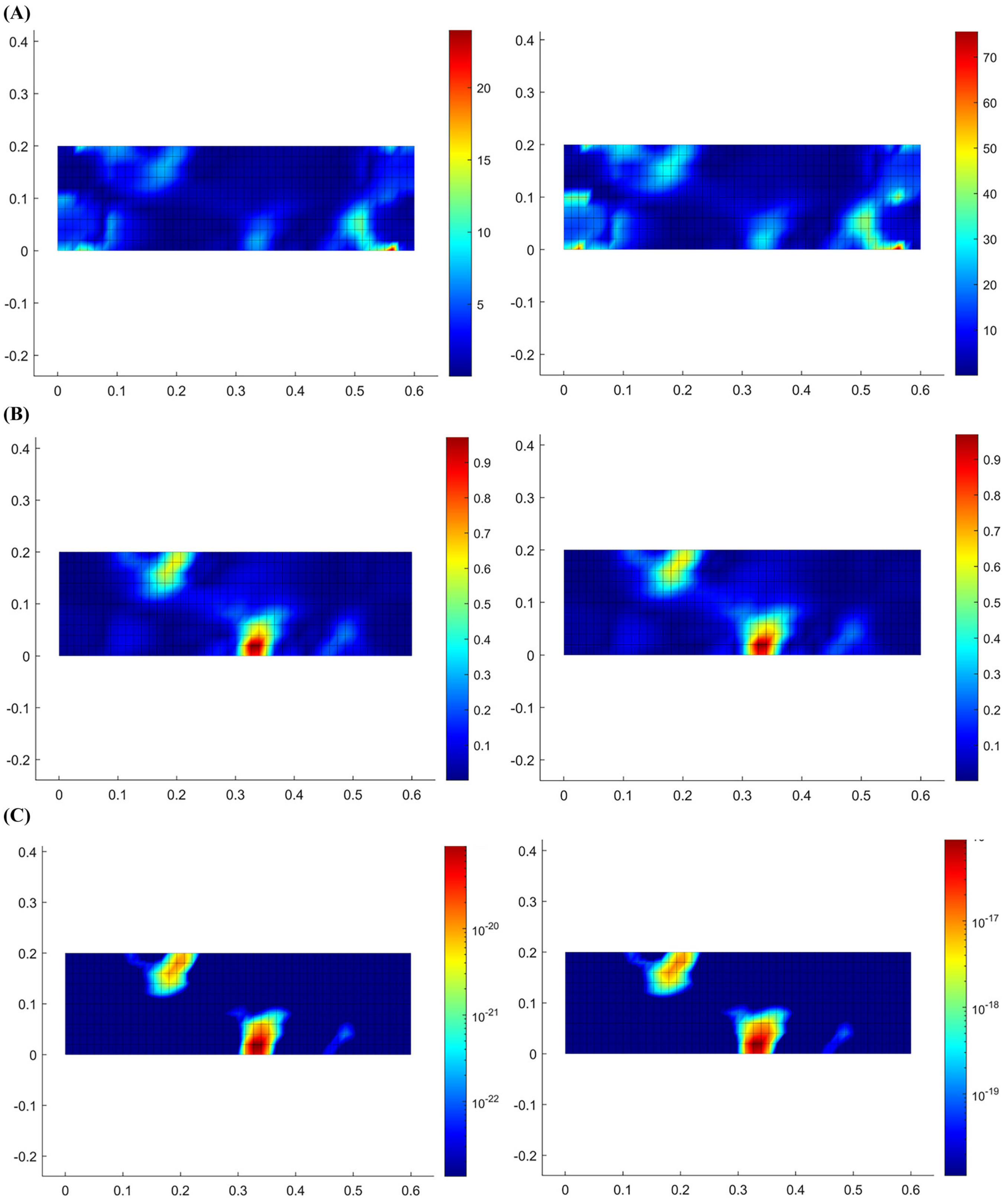

FIGURE 30 | Fine iFEM mesh—two-fine-arrays sensor configuration by considering 10% (left column) and 40% (right column) thickness reduction. Row (A), row (B), and row (C) show PDP, RDP, and LDP, respectively. iFEM, inverse finite element method; LDP, logarithmic damage parameter; PDP, percentage damage parameter; RDP, relative damage parameter.

can be installed on the determined sensor locations. Depending on the application and environment, it may be necessary to protect sensors to function properly and collect accurate data. Please note that the current study assumes that there is no initial damage in the structure. Because of this reason, any significant or abrupt change allows the iFEM methodology to detect the damage occurrence. However, the method can also be applicable to existing structures that are already exposed and damaged. In

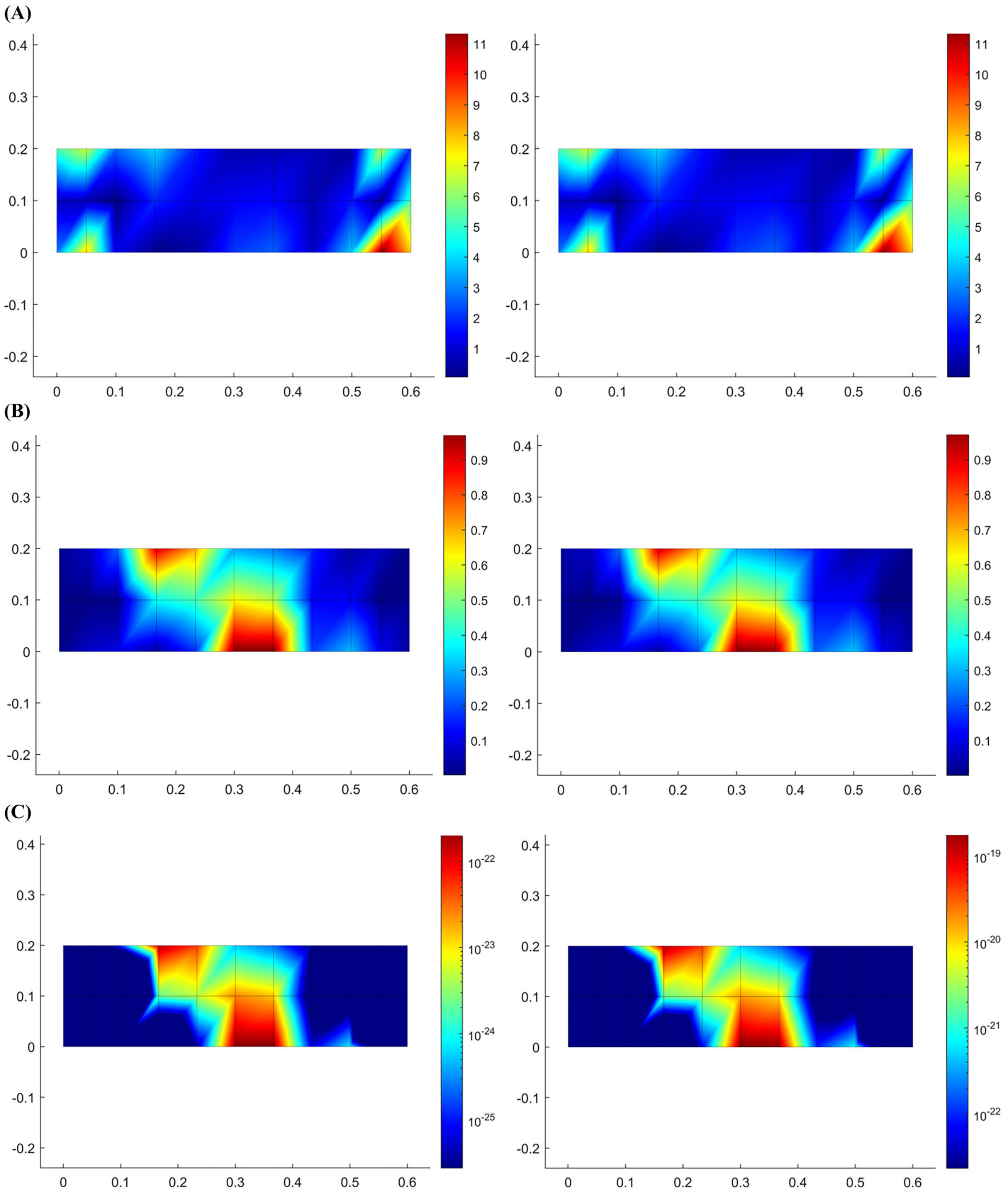

FIGURE 31 | Coarse iFEM mesh—two-coarse-arrays sensor configuration by considering 10% (left column) and 40% (right column) thickness reduction. Row (A), row (B), and row (C) show PDP, RDP, and LDP, respectively. iFEM, inverse finite element method; LDP, logarithmic damage parameter; PDP, percentage damage parameter; RDP, relative damage parameter.

this case, the existing damage should be defined at the beginning of the analysis. In addition, the presence of a coating on the steel was not considered. However, it can be considered as part of the inverse-shell formulation utilized in this study. Finally, a 3D model can also be an alternative option rather than using shell elements. However, similar to the regular finite element method, this can lead to an increase in the number of elements, which can then lead to an increase in the number of sensors.

Acknowledgments

We would like to thank Babcock International Group for its financial support of the project.

Conflicts of Interest

The authors declare no conflicts of interest.

Data Availability Statement

The data that support the findings of this study are available from the corresponding author upon reasonable request.

References

1. A. S. Katsoudas, N. E. Silionis, and K. N. Anyfantis, "Structural Health Monitoring for Corrosion Induced Thickness Loss in Marine Plates Subjected to Random Loads," *Ocean Engineering* 273 (2023): 114037.

2. C. H. Tan, Y. G. Shee, B. K. Yap, and F. R. M. Adikan, "Fiber Bragg Grating Based Sensing System: Early Corrosion Detection for Structural Health Monitoring," *Sensors and Actuators, A: Physical* 246 (2016): 123–128.

3. G. E. Simmers, Jr, H. A. Sodano, G. Park, and D. J. Inman, "Detection of Corrosion Using Piezoelectric Impedance-Based Structural Health Monitoring," *AIAA Journal* 44, no. 11 (2006): 2800–2803.

4. A. Tessler and J. L. Spangler, "A Least-Squares Variational Method for Full-Field Reconstruction of Elastic Deformations in Shear-Deformable Plates and Shells," *Computer Methods in Applied Mechanics and Engineering* 194, no. 2–5 (2005): 327–339.

5. J. Wang, L. Ren, R. You, T. Jiang, Z. Jia, and Gx Wang, "Experimental Study of Pipeline Deformation Monitoring Using the Inverse Finite Element Method Based on the iBeam3 Element," *Measurement* 184 (2021): 109881.

6. A. Tessler, R. Roy, M. Esposito, C. Surace, and M. Gherlone, "Shape Sensing of Plate and Shell Structures Undergoing Large Displacements Using the Inverse Finite Element Method," *Shock and Vibration* 2018, no. 1 (2018): 8076085.

7. R. Roy and M. Gherlone, "Delamination and Skin-Spar Debond Detection in Composite Structures Using the Inverse Finite Element Method," *Materials* 16, no. 5 (2023): 1969.

8. P. Cerracchio, M. Gherlone, and A. Tessler, "Real-Time Displacement Monitoring of a Composite Stiffened Panel Subjected to Mechanical and Thermal Loads," *Meccanica* 50 (2015): 2487–2496.

9. A. Kefal, A. Tessler, and E. Oterkus, "An Enhanced Inverse Finite Element Method for Displacement and Stress Monitoring of Multilayered Composite and Sandwich Structures," *Composite Structures* 179 (2017): 514–540.

10. I. D. Craiu and M. Nedelcu, "Combining iFEM and GBT for Accurate Shape Sensing and Damage Detection in Truncated Conical Shells With Circular Cross-Section," *Ocean Engineering* 311 (2024): 118811.

11. C. De Mooij, M. Martinez, and R. Benedictus, "iFEM Benchmark Problems for Solid Elements," *Smart Materials and Structures* 28, no. 6 (2019): 065003.

12. G. Chen, X. Wang, Q. Zhu, et al., "Reconstruction of Multi-Load Strain Field of Ship Stiffened Plate Based on iFEM and Analysis of Influencing Factors of Reconstruction Accuracy," *Journal of Marine Science and Engineering* 13, no. 2 (2025): 350.

13. F. Zhao, R. Du, J. Wang, F. Zhang, and B. Hong, "Geometrically Nonlinear Shape Sensing of Anisotropic Composite Beam Structure Using iFEM Algorithm and Third-Order Shear Deformation Theory," *Composite Structures* 322 (2023): 117364.

14. A. Kefal, E. Oterkus, A. Tessler, and J. L. Spangler, "A Quadrilateral Inverse-Shell Element With Drilling Degrees of Freedom for Shape Sensing and Structural Health Monitoring," *Engineering Science and Technology, an International Journal* 19, no. 3 (2016): 1299–1313.

15. A. Kefal and E. Oterkus, "Displacement and Stress Monitoring of a Panamax Containership Using Inverse Finite Element Method," *Ocean Engineering* 119 (2016): 16–29.

16. A. Kefal and E. Oterkus, "Displacement and Stress Monitoring of a Chemical Tanker Based on Inverse Finite Element Method," *Ocean Engineering* 112 (2016): 33–46.

17. A. Kefal, J. B. Mayang, E. Oterkus, and M. Yildiz, "Three Dimensional Shape and Stress Monitoring of Bulk Carriers Based on iFEM Methodology," *Ocean Engineering* 147 (2018): 256–267.

18. M. Li, A. Kefal, E. Oterkus, and S. Oterkus, "Structural Health Monitoring of an Offshore Wind Turbine Tower Using iFEM Methodology," *Ocean Engineering* 204 (2020): 107291.

19. I. Khalid, Z. A. Qureshi, H. A. Khan, S. Oterkus, and E. Oterkus, "A Quadrilateral Inverse Plate Element for Real-Time Shape-Sensing and Structural Health Monitoring of Thin Plate Structures," *Computers & Structures* 305 (2024): 107551.

20. A. Kefal and E. Oterkus, "Isogeometric iFEM Analysis of Thin Shell Structures," *Sensors* 20, no. 9 (2020): 2685.

21. Y. Dirik, S. Oterkus, and E. Oterkus, "Isogeometric Mindlin–Reissner Inverse-Shell Element Formulation for Complex Stiffened Shell Structures," *Ocean Engineering* 305 (2024): 118028.

22. P. Lancaster and S. Kestutis, *Curve and Surface Fitting. An Introduction* (Academic Press, 1986).

23. A. Tessler, H. R. Riggs, C. E. Freese, and G. M. Cook, "An Improved Variational Method for Finite Element Stress Recovery and a Posteriori Error Estimation," *Computer Methods in Applied Mechanics and Engineering* 155, no. 1–2 (1998): 15–30.

24. A. Tessler, H. R. Riggs, and M. Dambach, "A Novel Four-Node Quadrilateral Smoothing Element for Stress Enhancement and Error Estimation," *International Journal for Numerical Methods in Engineering* 44, no. 10 (1999): 1527–1543.

25. M. Li, A. Kefal, B. C. Cerik, and E. Oterkus, "Dent Damage Identification in Stiffened Cylindrical Structures Using Inverse Finite Element Method," *Ocean Engineering* 198 (2020): 106944.

26. M. F. Granata, "Effects of Corrosion on a Steel Bowstring Bridge in Marine Environment: A Case-Study of Assessment and Retrofit," *Bridge Structures* 16, no. 4 (2021): 121–137.